CANCER

Combination of metabolic intervention and T cell therapy enhances solid tumor immunotherapy

Meixi Hao*, Siyuan Hou*, Weishuo Li, Kaiming Li, Lingjing Xue, Qifan Hu, Lulu Zhu, Yue Chen, Hongbin Sun, Caoyun Ju†, Can Zhang†

Treatment of solid tumors with T cell therapy has yielded limited therapeutic benefits to date. Although T cell therapy in combination with proinflammatory cytokines or immune checkpoints inhibitors has demonstrated preclinical and clinical successes in a subset of solid tumors, unsatisfactory results and severe toxicities necessitate the development of effective and safe combinatorial strategies. Here, the liposomal avasimibe (a metabolism-modulating drug) was clicked onto the T cell surface by lipid insertion without disturbing the physiological functions of the T cell. Avasimibe could be restrained on the T cell surface during circulation and extravasation and locally released to increase the concentration of cholesterol in the T cell membrane, which induced rapid T cell receptor clustering and sustained T cell activation. Treatment with surface anchor-engineered T cells, including mouse T cell receptor transgenic CD8$^+$ T cells or human chimeric antigen receptor T cells, resulted in superior antitumor efficacy in mouse models of melanoma and glioblastoma. Glioblastoma was completely eradicated in three of the five mice receiving surface anchor-engineered chimeric antigen receptor T cells, whereas mice in other treatment groups survived no more than 64 days. Moreover, the administration of engineered T cells showed no obvious systemic side effects. These cell-surface anchor-engineered T cells hold translational potential because of their simple generation and their safety profile.

INTRODUCTION

T cell therapy has demonstrated great clinical and preclinical successes in treatment of hematological malignancies (*1*, *2*). Despite these encouraging results, treatment of solid tumors with T cells yields limited therapeutic benefits (*3*). Most studies have focused on the coadministration of proinflammatory cytokines or immune checkpoint inhibitors with T cells to boost efficacy (*4*–*8*). However, unsatisfactory results and severe side effects observed in some patients necessitate the development of effective and safe combination therapies (*9*, *10*). Previous studies have demonstrated that the suppressive metabolic state of the oxygen- and nutrient-deprived tumor microenvironment impedes T cell infiltration, survival, and effector function, which likely compromises the therapeutic benefit of solid tumor T cell therapy (*11*, *12*). T cell metabolism involves multiple diverse pathways, offering a breadth of potential intervention targets (*12*). For example, T cell function is dependent on the amount of cholesterol on cell membrane to cluster T cell receptors (TCRs) and form an immunological synapse (*13*–*15*). Therefore, modulation of cholesterol metabolism in combination with T cell therapy holds potential for improving solid tumor immunotherapy.

Avasimibe (Ava), an inhibitor of the cholesterol-esterification enzyme acetyl-CoA acetyltransferase 1 (ACAT1), elevates plasma membrane cholesterol concentrations, which, in turn, promote TCR clustering and thus improve effector function of T cells (*16*). We therefore hypothesized that combining Ava with T cell therapy would boost solid tumor immunotherapy. However, the pharmacokinetics and biodistribution of Ava are different from those of T cells, which imposes a challenge on optimizing the two as a combination therapy (*17*–*20*). Thus, there is a need to develop promising combinatorial technologies that maximize both individual therapies.

Genetically engineered T cells can serve as a living factory to produce designed protein drugs (*21*–*23*). However, heterogeneous expression of engineered proteins, combined with potential for toxicity, reduces the efficacy of this strategy (*24*, *25*). In addition, small molecular drugs cannot be manipulated in this genetic manner. An alternative to genetic engineering can be accomplished by backpacking nanoparticulated drugs onto the T cell surface via chemical conjugation or ligand-receptor biorecognition. This strategy has been shown to augment T cell function and widen the therapeutic window of combined drugs (*26*–*28*). Of note, backpacking strategies may impair the physiological functions of T cells. These effects can be due to long-term occupation of the functional biomolecules on the T cell membrane or due to changes to the glycometabolism of the T cell (*27*–*31*). Thus, technology to backpack nanoparticulated drugs onto the T cell surface can be further improved to reduce the impact of backpacking on the function of T cells.

Here, inspired by glycosylphosphatidylinositol-anchored proteins on the plasma membrane and click chemistry (*32*–*34*), we developed an alternative strategy to backpack drugs on the T cell surface by T cell–surface anchor-engineering technology. Specifically, we introduced functional tetrazine (Tre) groups onto the T cell surface via lipid insertion in the cell membrane. Next, liposomal Ava containing bicyclo [6.1.0] nonyne (BCN) groups was clicked onto the cell surface without disturbing the physiological functions of engineered T cells. We show that the liposomal Ava was retained on the T cell surface during circulation as well as extravasation and locally released to increase cholesterol in the T cell membrane. The increased cholesterol promoted rapid TCR clustering and sustained T cell activation. Last, we found that engineering TCR transgenic CD8$^+$ T cells and chimeric antigen receptor T cells (CAR T cells) to carry liposomal Ava showed superior antitumor efficacy in mouse models of melanoma and glioblastoma.

State Key Laboratory of Natural Medicines, Jiangsu Key Laboratory of Drug Discovery for Metabolic Diseases, Center of Advanced Pharmaceuticals and Biomaterials, China Pharmaceutical University, Nanjing 210009, P.R. China.
*These authors contributed equally to this work.
†Corresponding author. Email: zhangcan@cpu.edu.cn (C.Z.); jucaoyun@cpu.edu.cn (C.J.)

RESULTS

Design and generation of cell-surface anchor-engineered T cells

Cell-surface anchor-engineering of T cells involved two steps: inserting the anchor of tetrazine-bearing, two-tailed lipids into the lipid bilayers of T cell membrane via hydrophobic interactions and the subsequent biorthogonal click reaction of cell-surface tetrazines with BCN-containing liposomal Ava, as illustrated in Fig. 1A. To this end, tetrazine-bearing, two-tailed lipids [1,2-distearoyl-*sn*-glycero-3-phosphoethanolamine-*N*-amino(polyethylene glycol)5000-tetrazine (DSPE-PEG$_{5k}$-Tre)] and complementary BCN-derived lipids [1,2-distearoyl-*sn*-glycero-3-phosphoethanolamine-BCN (DSPE-BCN)] were designed and synthesized (fig. S1), and structures were verified by proton nuclear magnetic resonance (^{1}H-NMR) and mass spectrometry (MS). DSPE-PEG$_{5k}$-Tre rapidly reacted with DSPE-BCN at room temperature in phosphate-buffered saline (PBS) as measured by ultraviolet spectroscopy (fig. S2A). We used DSPE-BCN to prepare BCN-containing liposomal Ava (BCN-Lipo-Ava) based on our previous work (*35*). The generated BCN-Lipo-Ava displayed an average particle size of 91.5 nm with a uniform spheroid shape, as suggested by transmission electron microscopy (TEM) images (fig. S2B). The loading capacity and entrapment efficiency of BCN-Lipo-Ava for Ava were measured at 2.3 and 89.1%, respectively. Moreover, BCN-Lipo-Ava remained stable under physiological conditions without detectable accumulations for at least 24 hours (fig. S2C). The resulting BCN-Lipo-Ava rapidly and mildly reacted with DSPE-PEG$_{5k}$-Tre at room temperature in PBS within 0.5 hours (fig. S2D), similar to the reaction of DSPE-PEG$_{5k}$-Tre and DSPE-BCN (fig. S2A). Together, these findings demonstrated the potential of this anchor-click technology to engineer living cells.

To develop effective and biocompatible anchor-click conditions for living-cell engineering, we examined a number of cellular anchor-click parameters, including anchor-click feeding concentrations and time. No reduction in T cell viability was observed when incubated with DSPE-PEG$_{5k}$-Tre (100 μg/ml) and BCN-Lipo-Ava (Ava concentration: 100 μg/ml) up to 24 hours, indicating the cytocompatibility of these two modules (fig. S3, A and B). When the feeding concentration of BCN-Lipo-Ava was fixed at 100 μg/ml, the amount of Ava in T-Tre/BCN-Lipo-Ava cells increased from 1 to 4 μg per million cells and then plateaued as the feeding amount of anchor module-DSPE-PEG$_{5k}$-Tre increased. The feeding amount of DSPE-PEG$_{5k}$-Tre plateaued at 80 μg/ml (fig. S3, C and D). Last, we found that the time of anchor and click both positively correlated to the amount of Ava in T-Tre/BCN-Lipo-Ava cells before reaching a plateau at 10 min for the anchor and 30 min for the click (fig. S3, E and F). Moving forward, unless it is specifically stated, the feeding amounts of DSPE-PEG$_{5k}$-Tre and BCN-Lipo-Ava were set as 80 and 100 μg/ml, and the incubation times of anchor and click were fixed at 10 and 30 min, respectively. With this strategy, the total number of liposomes anchored on the surface of T cells was about 275 liposomes per T cell, with nearly 4 μg of Ava per million cells (table S1 and fig. S3C).

Having demonstrated the cytocompatibility and efficacy of our anchor-click–based living-cell engineering, we next characterized the resulting T-Tre/BCN-Lipo cells. To this end, DSPE-PEG$_{5k}$-Tre and BCN-Lipo were tagged by fluorescein isothiocyanate and rhodamine, respectively (FITC-DSPE-PEG$_{5k}$-Tre and BCN-Lipo-RhoB). Fluorescence-tagged lipids and liposomes without clickable groups (FITC-DSPE-PEG$_{5k}$ and Lipo-RhoB) were also prepared as controls. As displayed in Fig. 1B, T-Tre/BCN-Lipo-RhoB cells showed the highest fluorescence intensity in comparison to T/BCN-Lipo-RhoB cells and T-Tre/Lipo-RhoB cells, indicating that the anchoring of liposomes onto the T cell surface was due to DSPE-PEG$_{5k}$-Tre anchor and the subsequent click reaction rather than physical absorption. Furthermore, as evidenced by fluorescent images of T-FITC-Tre/BCN-Lipo-RhoB cells along with the corresponding correlation coefficients (Fig. 1, C and D), FITC-DSPE-PEG$_{5k}$-Tre colocalized with both the T cell surface marker CD8 and BCN-Lipo-RhoB, suggesting that DSPE-PEG$_{5k}$-Tre successfully anchored into the cell surface and underwent the click reaction of Tre and BCN. In contrast, no such colocalized signal was observed in T-FITC/BCN-Lipo-RhoB cells because of the lack of Tre groups inserted on the cell surface. To better visualize the morphology of T-Tre/BCN-Lipo cells, we obtained scanning electron microscopy (SEM) images. Here, we used BCN-modified gold nanoparticles instead of BCN-Lipo, because the structure of BCN-Lipo was fragile to dehydration during the preparation of SEM samples. As shown in Fig. 1E, gold nanoparticles were observed on the T cell surface as indicated by red arrows.

Next, we investigated the stability and retention of the BCN-Lipo-Ava on the cell surface. RhoB-tagged BCN-Lipo-Ava stayed attached on the surface of T-Tre/BCN-Lipo-Ava cells for up to 4 days, as demonstrated by confocal microscopy imaging (Fig. 1F). Retention of RhoB-tagged BCN-Lipo-Ava likely resulted from the strong hydrophilicity and steric hindrance of PEG chain in the anchor module-DSPE-PEG$_{5k}$-Tre. About 50 and 30% of initial anchoring liposomes were retained on T-Tre/BCN-Lipo-Ava cells at days 2 and 4, respectively, as measured by flow cytometry (Fig. 1G and fig. S4). In addition, about 50% of the backpacked Ava was stably retained on the surface of T-Tre/BCN-Lipo-Ava cells after 48-hour culture in fetal bovine serum (FBS)–free or 50% FBS–containing RPMI 1640 medium at 37°C (Fig. 1, H and I). Together, these data demonstrate superior stability of T-Tre/BCN-Lipo-Ava cells with respect to not only the retention of liposomes on the cell surface but also the entrapment of Ava in the retained liposomes.

Key physiological functions of T-Tre/BCN-Lipo-Ava cell in vitro

The viability of T-Tre/BCN-Lipo-Ava cells was monitored over 10 days. As shown in Fig. 2A, the viability of T-Tre/BCN-Lipo-Ava cells was higher than 80% during all 10 days. In addition, the frequency of apoptosis in T-Tre/BCN-Lipo-Ava cells was measured at 2.81% on day 10 (fig. S5). Together, these results demonstrated unimpaired viability of engineered T-Tre/BCN-Lipo-Ava cells. The in vitro expansion of T-Tre/BCN-Lipo-Ava cells after stimulation with anti-CD3/CD28 antibodies was comparable to that of unmodified T cells, and this robust and unimpaired proliferative capacity of T-Tre/BCN-Lipo-Ava cell was further verified by dilution of carboxyfluorescein diacetate succinimidyl ester (CFSE) (Fig. 2, B and C).

Next, we observed no reduction in trans-endothelium migration capacity of T-Tre/BCN-Lipo-Ava cells compared with unmodified T cells (Fig. 2D). We also compared chemotaxis of T-Tre/BCN-Lipo-Ava cells to unmodified T cells using monocyte chemoattractant protein–1 (MCP-1) as a chemoattractant (*27*). As presented in Fig. 2E, T-Tre/BCN-Lipo-Ava cells and unmodified T cells migrated comparably in response to increasing concentrations of MCP-1. These results suggest that T-Tre/BCN-Lipo-Ava cells maintain an intact chemotaxis capacity. Given that T-Tre/BCN-Lipo-Ava cells

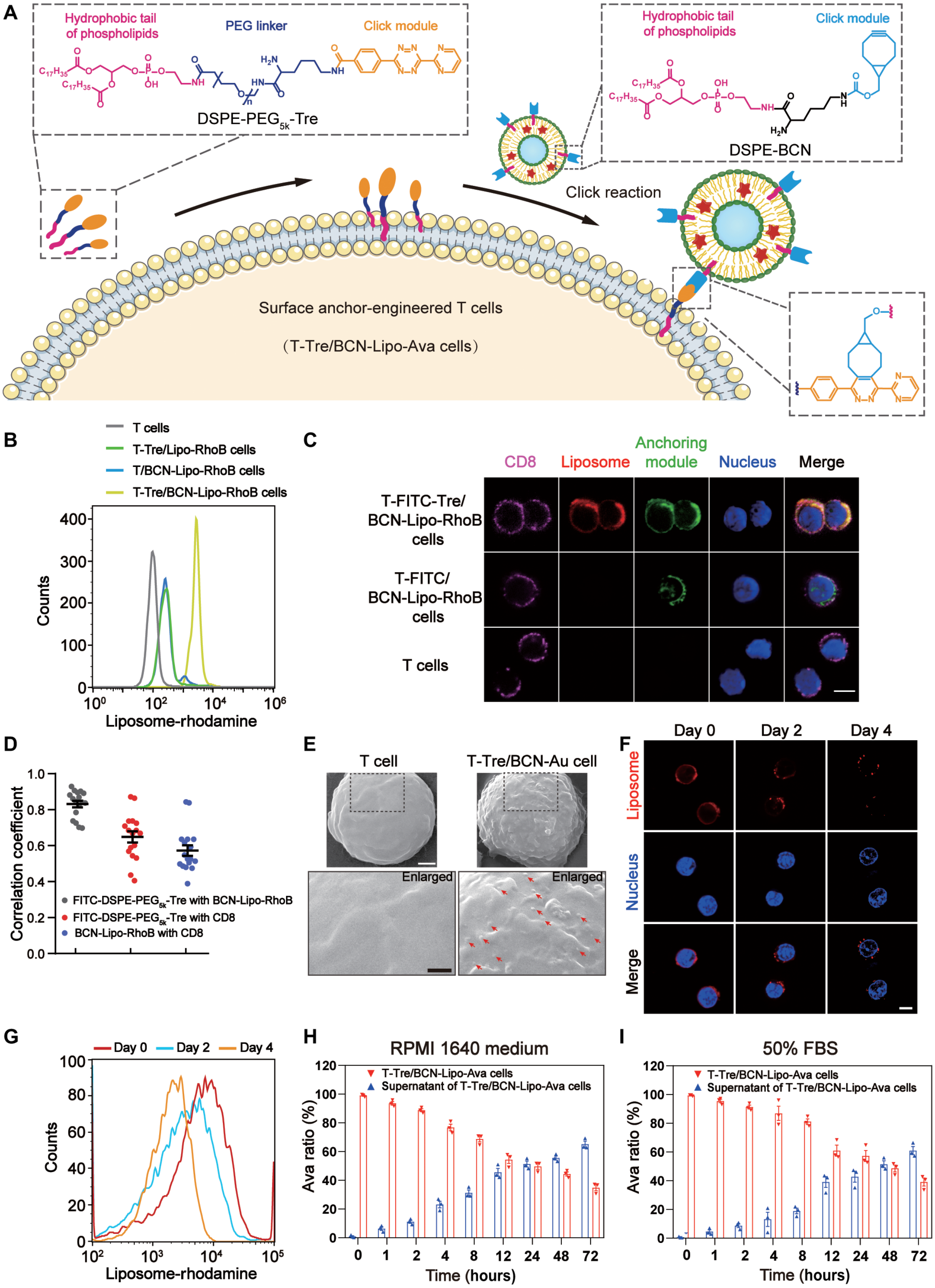

Fig. 1. Generation and characterizations of T-Tre/BCN-Lipo-Ava cells. (**A**) Schematic diagram of generation of cell-surface anchor-engineered T cells (referred as T-Tre/BCN-Lipo cells). (**B**) Flow cytometry analysis of T-Tre/Lipo-RhoB cells, T/BCN-Lipo-RhoB cells, and T-Tre/BCN-Lipo-RhoB cells, using T cells as the control (*n* = 3 samples per group). (**C**) Fluorescence images of T-FITC-Tre/BCN-Lipo-RhoB cells, T-FITC/BCN-Lipo-RhoB cells, and T cells. All cells were costained with APC-Cy7–conjugated anti-CD8α antibody and Hoechst 33342. Scale bar, 5 μm (*N* = 2 independent experiments). (**D**) Pearson's correlation coefficients for FITC-DSPE-PEG$_{5k}$-Tre and BCN-Lipo-RhoB, FITC-DSPE-PEG$_{5k}$-Tre and APC-Cy7-anti-CD8α, and BCN-Lipo-RhoB and APC-Cy7-anti-CD8α, as shown in (C) (*n* = 17 cells). Values >0.5 indicate colocalization of two fluorescent signals. (**E**) SEM of a T-Tre/BCN-Au cell and a T cell. Red arrows indicate BCN-Au nanoparticles. White scale bar, 1 μm. Black scale bar, 500 nm. (**F**) Confocal microscopy images of T-Tre/BCN-Lipo-Ava cells after in vitro expansion for 2 and 4 days. Scale bar, 5 μm (*N* = 2 independent experiments). (**G**) Flow cytometry analysis of T-Tre/BCN-Lipo-RhoB cell expansion at 37°C for 2 and 4 days, using freshly prepared T-Tre/BCN-Lipo-RhoB cells as control (*n* = 3 samples per group). (**H** and **I**) Percentages of Ava in T-Tre/BCN-Lipo-Ava cells, which were cultured in RPMI 1640 medium containing (H) no or (I) 50% FBS for different incubation times (*n* = 3 samples per group). Data presented as means ± error bars denote SEM.

could reshape their cytoskeletons and cell membranes during migration (*36*), we investigated whether this remodeling led to a loss of backpacked Ava. Therefore, we quantified the relative amount of Ava on the surface of migrated T-Tre/BCN-Lipo-Ava cells, finding only a modest reduction (fig. S6, A to C) that still fulfilled the dosage requirement for in vivo application (*16*).

Moreover, we found that the surface expressions of the early T cell activation marker CD69 (*37*–*39*) was low on both T-Tre/BCN-Lipo-Ava

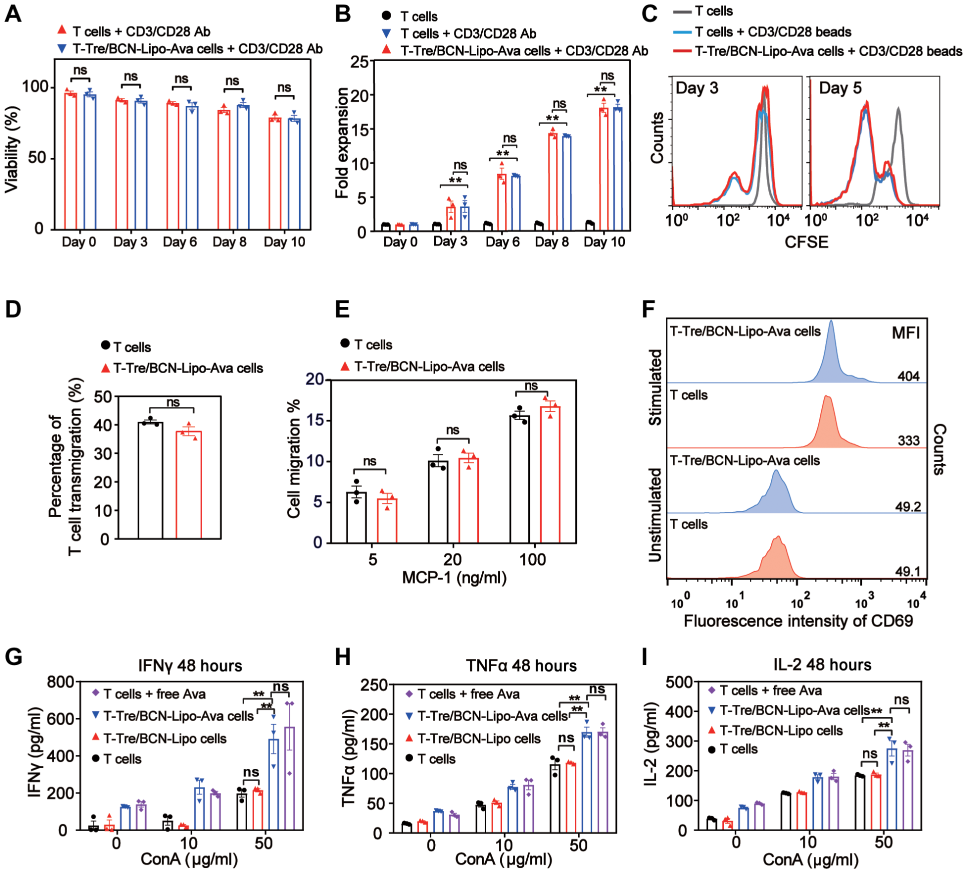

Fig. 2. T-Tre/BCN-Lipo-Ava cells maintain key physiological functions of T cells. (**A**) Viability of T-Tre/BCN-Lipo-Ava cells for up to 10 days after stimulation with anti-CD3 and anti-CD28 antibodies (CD3/CD28 Ab) ($n = 3$ samples per group). (**B**) In vitro expansion of T-Tre/BCN-Lipo-Ava cells after stimulation. Naive and stimulated T cells were used as controls ($n = 3$ samples per group). (**C**) Representative flow cytometry histograms of T-Tre/BCN-Lipo-Ava cells after stimulation using T cells with and without stimulation as controls ($n = 3$ samples per group). (**D** and **E**) Transwell assay of (D) trans-endothelium and (E) chemotaxis migration behaviors of T-Tre/BCN-Lipo-Ava cells using MCP-1 as the chemoattractant. (**F**) Flow cytometry analysis of cell surface CD69 expression with and without stimulation. MFI, mean fluorescence intensity. Secretion of inflammatory cytokines including (**G**) IFNγ, (**H**) TNFα, and (**I**) IL-2 was measured by ELISA after stimulation for 48 hours with concanavalin A (ConA) ($n = 3$ samples per group). Data were analyzed by one-way ANOVA test with Tukey's correction. Error bars denote SEM. $^{**}P < 0.01$. ns denotes no significant difference.

cells and unmodified T cells without stimulation and increased to the same extent in response to anti-CD3/CD28 antibody stimulation, suggesting that the condition of T-Tre/BCN-Lipo-Ava cells was dependent on exogenous immune stimuli rather than the engineering process or reagents (Fig. 2F). In addition, the secretion of interleukin-2 (IL-2), interferon γ (IFNγ), and tumor necrosis factor α (TNFα) by concanavalin A (ConA)–stimulated T-Tre/BCN-Lipo cells was comparable to that of unmodified T cells, but less than that of T-Tre/BCN-Lipo-Ava cells and T cells plus free Ava (Fig. 2, G to I, and fig. S7), indicating that the backpacked Ava could improve T cell function, whereas the insertion of BCN-Lipo had no effect on cytokine secretion.

We further examined the basal energy metabolism of T-Tre/BCN-Lipo-Ava cells. Mitochondrial oxygen consumption rate (OCR) and extracellular acidification rate (ECAR) of T-Tre/BCN-Lipo-Ava cells and unconjugated T cells were comparable (fig. S8), confirming that the engineering technology did not affect basal oxidative phosphorylation and glycolysis.

Despite our findings that the survival, chemotaxis ability, activation, cytokine secretion, and basal energy metabolism of T-Tre/BCN-Lipo-Ava cells were unaffected by engineering, the influence of engineering on other proteins related to T cell function was unclear. To clarify this, we performed MS to examine T cell proteome alterations. We compared the overall proteome changes between T-Tre/BCN-Lipo cells (without drug loading) and unconjugated T cells by Tandem Mass Tag (TMT)–based quantitative proteomics. We found that only 7 of 7226 proteins analyzed showed more than 1.5-fold change in abundance, suggesting that very few proteins were affected by the cell-surface anchor-engineering. Of note, the abundance of most proteins involved in TCR signaling, T cell activation, T cell proliferation, and immune effector process remained unchanged (fig. S9), suggesting that central molecular signatures related to T cell function remained unaffected.

The antitumor responses of T-Tre/BCN-Lipo-Ava cell in vitro

To evaluate the cytotoxicity of T-Tre/BCN-Lipo-Ava cells toward tumor cells, we cocultured $CD8^+$ T cells isolated from pmel-1 TCR transgenic mice, which have a TCR specific for the mouse homolog (pmel) of human premelanosome protein gp100 (*40*), with B16F10 melanoma cells at an effector:target ratio of 10:1. As shown in Fig. 3A, T-Tre/BCN-Lipo-Ava cells killed nearly 80% of cocultured B16F10 cells at 48 hours compared to 50% of unconjugated T cells. In contrast, pretreatment of $CD8^+$ T cells with Ava (pre-Ava T cells) only yielded modest toxicity against B16F10 cells, whereas T cells plus free Ava demonstrated comparable toxicity to that of T-Tre/BCN-Lipo-Ava cells. We hypothesized that the duration of Ava action led to improved cytotoxicity of T cells through inhibiting ACAT1 expression. However, it was reported that Ava could directly inhibit the growth of tumor cells by targeting tumor cell–derived ACAT1 (*41*). To clarify whether the decline in tumor progression is driven by the potentiated cytotoxic T cell response rather than the higher concentration of Ava in the tumor environment, we assessed expression of ACAT1 in B16F10 melanoma and LN-229 glioblastoma cells in culture and in established tumors (fig. S10, A and B). B16F10 melanoma and LN-229 glioblastoma cells expressed less ACAT1 protein compared with PC-3 prostate cancer cells, which have been previously reported to express high ACAT1 protein (*41*). Treatment with Ava at a concentration under 10 μM did not affect viability of B16F10 and LN-229 cells (fig. S10, C and D), whereas the viability of PC-3 cells with high expression of ACAT1 protein was decreased (fig. S10E), confirming

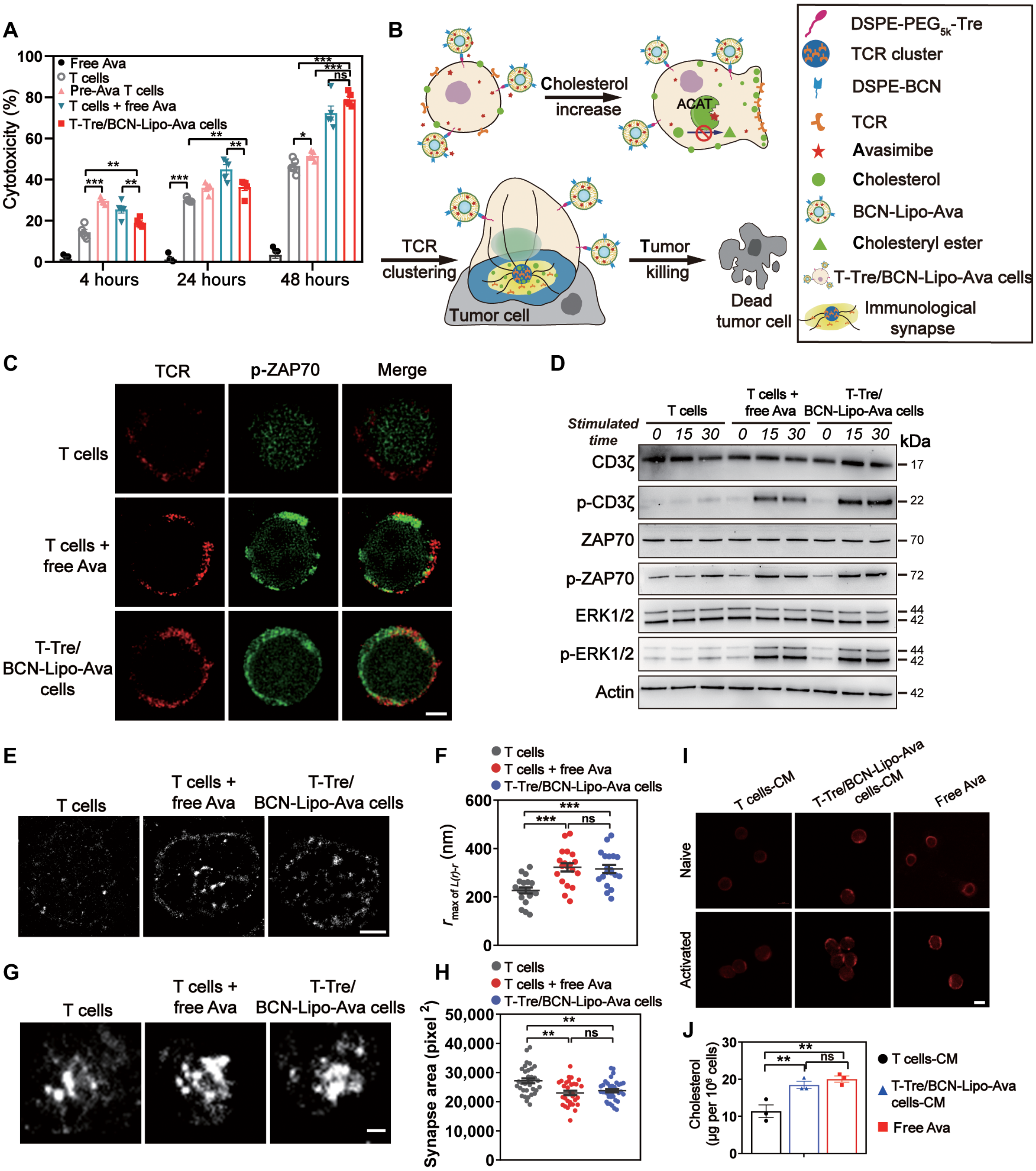

Fig. 3. T-Tre/BCN-Lipo-Ava cells display enhanced TCR clustering and immunological synapse formation, with improved antitumor responses. (**A**) Cytotoxicity against B16F10 tumor cells ($n = 4$ samples per group) as measured by release of lactate dehydrogenase. (**B**) Proposed mechanism of enhanced antitumor responses of T-Tre/BCN-Lipo-Ava cells. (**C**) Representative fluorescence images of TCR and p-ZAP70 after stimulation with anti-CD3/CD28 antibodies using stimulated emission depletion microscopy. All the cells were stained with anti–TCRβ–Alexa Fluor 647 and anti–pZAP70–Alexa Fluor 488. Scale bar, 2 μm. (**D**) Immunoblotting of proximal and downstream TCR signaling molecules after stimulation with anti-CD3/CD28 antibodies ($N = 3$ independent experiments). (**E**) Super-resolution STORM images and (**F**) quantification of TCR clustering. Scale bar, 2 μm. Graph shows *r* value at the maximal $L(r) - r$ value of Ripley's K-function curves ($n = 20$ cells), representing the cluster size with the highest probability, where $L(r) - r$ represents the efficiency of molecule clustering, and *r* represents cluster radius ($N = 2$ independent experiments). (**G**) Total internal reflection fluorescence microscopy images and (**H**) quantification of the immunological synapse size. Total synapse areas were quantified using the entire signal from each field. Scale bar, 2 μm. (**I**) Fluorescence microscopy images of Filipin III–stained naive or activated CD8$^+$ T cells incubated with T-Tre/BCN-Lipo-Ava cell-CM or T cell-CM for 12 hours. Scale bar, 5 μm ($N = 2$ independent experiments). (**J**) Quantification of plasma membrane cholesterol content in CD8$^+$ T cells using an oxidation-based method. Data were analyzed by one-way ANOVA test with Tukey's correction. Error bars denote SEM. *$P < 0.05$, **$P < 0.01$, ***$P < 0.001$. ns denotes no significant difference.

that inhibition of cancer cell growth in tumors with low expression of ACAT1 is not driven by the cytotoxicity of Ava to cancer cells directly, but rather by potentiated T cell antitumor responses.

Moreover, we investigated whether the augmented antitumor responses of T-Tre/BCN-Lipo-Ava cell were due to enhanced TCR clustering and immunological synapse formation mediated by

Ava-induced increased membrane cholesterol content (Fig. 3B). To accomplish this, we first measured the cholesterol content of engineered T cells and found that backpacked Ava on T-Tre/BCN-Lipo-Ava cells increased cholesterol concentration (fig. S11). Consistent with a previous report (*16*), the increased cholesterol content was due to the Ava-inhibited conversion of cholesterol to cholesteryl esters and the modestly enhanced cholesterol biosynthesis (fig. S12). Then, we assessed whether increased cholesterol promotes antitumor responses by adding or depleting cholesterol on the plasma membrane of T cells. The results showed that addition of plasma membrane cholesterol led to improved effector function, which was consistent with enhanced effector function induced by free Ava or backpacked Ava (fig. S13, A to C), whereas depletion of plasma membrane cholesterol by incubating cells with methyl-β-cyclodextrin (*16*) led to impaired effector function of T-Tre/BCN-Lipo-Ava cell (fig. S13, D to F). These data further indicated a critical role of increased cholesterol in antitumor responses. Next, we examined TCR signaling by measuring downstream phosphorylated ζ-chain–associated protein kinase 70 (p-ZAP70) after stimulation in T-Tre/BCN-Lipo-Ava cells, control T cells, and T cells plus free Ava. As presented in Fig. 3C, a colocalized fluorescent signals was observed between the TCR and p-ZAP70 on the surface of T-Tre/BCN-Lipo-Ava cells. TCR signaling in T-Tre/BCN-Lipo-Ava cells was verified at the protein level by p-CD3, p-ZAP70, and p-ERK1/2 Western blots (Fig. 3D and fig. S14).

To further study the distribution and structure of TCRs on the T cell membrane, we used super-resolution imaging. Figure 3E and the corresponding quantitative results (Fig. 3F) showed that T-Tre/BCN-Lipo-Ava cells had a larger TCR microcluster compared to that of unconjugated T cells. Moreover, we investigated the formation of immunological synapse in T-Tre/BCN-Lipo-Ava cells to assess whether cholesterol is a component of the immunological synapse (*13*). Using total internal reflection fluorescence imaging, we found that, within the same experimental time, the TCRs of T-Tre/BCN-Lipo-Ava cells were more compact in the center of immunological synapse than those of unmodified T cells. The synapse of T-Tre/BCN-Lipo-Ava cells also had a smaller average area, indicating a faster maturation of immunological synapse compared with unmodified T cells (Fig. 3, G and H).

Having demonstrated that backpacked Ava could potentiate the antitumor responses of T-Tre/BCN-Lipo-Ava cells via improved TCR clustering and immunological synapse formation, likely in an autocrine-like manner, we next sought to figure out whether the backpacked Ava would potentiate the antitumor responses of endogenous, unmanipulated T cells in a paracrine-like manner, which may offer an additional benefit to engineered T cell treatment of solid tumors (*42*). In pursuit of this, we cultured unmanipulated T cells in T-Tre/BCN-Lipo-Ava cell– or T cell–conditioned medium (CM) and subsequently stained the cell membrane cholesterol by Filipin III (*16*). Fluorescent images presented in Fig. 3I suggest a higher content of cholesterol in the T cell membrane after culture in T-Tre/BCN-Lipo-Ava cell-CM. To confirm this finding, we quantified the plasma membrane–cholesterol content using an oxidation-based assay, which showed that the cholesterol content in T cell membrane doubled when cultured in T-Tre/BCN-Lipo-Ava cell-CM as compared with T cells cultured in T cell CM (Fig. 3J). Collectively, these findings suggest that backpacked Ava could inhibit the esterification of cholesterol in adoptively transferred T-Tre/BCN-Lipo-Ava cells and endogenous T cells in an autocrine- and paracrine-like manner, thereby maximizing antitumor responses of both transferred and endogenous T cells.

Combination of metabolic intervention and T cell therapy via T-Tre/BCN-Lipo-Ava cells against primary solid tumors

We first analyzed the homing of T-Tre/BCN-Lipo-Ava cells and accumulation of Ava in primary melanoma via adoptive transfer of pmel-1 CD8$^+$ T cells. The population of transferred T cells and Ava concentrations in the tumor were measured by flow cytometry and high-performance liquid chromatography (HPLC), respectively. We found that T-Tre/BCN-Lipo-Ava cells accumulated in the tumor with similar kinetics to unconjugated T cells, reaching peak infiltration by 48 hours, indicating that surface-anchoring did not affect the survival or trafficking of transferred T cells (fig. S15, A and B). The drug concentration of backpacked Ava also peaked at 48 hours after adoptive transfer (fig. S15C) at a 200-fold greater concentration than free Ava and at an 8-fold greater concentration than BCN-Lipo-Ava at 48 hours. Ava concentration remained high for at least 3 days after transfer. These data imply that BCN-Lipo-Ava remained stable and retained on the T cell surface during trafficking to tumors and might enhance antitumor T cell immunity because of the extended Ava action.

We next evaluated the antitumor efficacy of treatment with pmel-1 CD8$^+$ T-Tre/BCN-Lipo-Ava cells (T-Tre/BCN-Lipo-Ava cells) in vivo. B16F10 melanoma tumors were established via intradermal injection of B16F10 cells into wild-type C57BL/6 mice. The mice were randomly divided into nine groups, which were lymphodepleted with cyclophosphamide (2 mg/kg) and fludarabine (2 mg/kg) on day 6 and given two intravenous injections on post-tumor implantation days 8 and 14 with one of the following formulations: (i) saline, (ii) free Ava, (iii) BCN-Lipo-Ava, (iv) T cells, (v) T-Tre/BCN-Lipo cells, (vi) pre-Ava T cells, (vii) T cells plus free Ava, (viii) T cells plus BCN-Lipo-Ava, and (ix) T-Tre/BCN-Lipo-Ava cells (Fig. 4A). Tumor volume was monitored after treatment. T-Tre/BCN-Lipo-Ava cell–treated mice showed the slowest rate of tumor growth over 20 days (Fig. 4B). Tumors harvested from mice on day 20 were stained to analyze the expression of the proliferation marker Ki67 by immunohistochemistry. As presented in Fig. 4 (C and D), fewer Ki67-positive tumor cells were observed in T-Tre/BCN-Lipo-Ava cell–treated group. The number of Ki67-positive cells was half of those in T cell–treated mice and one-third of those in mice receiving free Ava. Consistent with growth and proliferation profiles of the analyzed tumors, 50% of mice in another cohort receiving T-Tre/BCN-Lipo-Ava cells survived for at least 63 days, compared to 28 days for saline-treated mice (Fig. 4E). Dual administration of T cells and BCN-Lipo-Ava inhibited tumor growth moderately compared with T-Tre/BCN-Lipo-Ava cells, with no mice surviving after 53 days (Fig. 4E). Even Ava-pretreated T cells (pre-Ava T cell) exhibited only moderate antitumor effects (Fig. 4E). In addition, none of the treatments caused loss of body weight (Fig. 4F) or tissue damage (figs. S16 to S20), and adoptive transfer of T-Tre/BCN-Lipo-Ava cells induced neither systemic cytokine release (IL-10, IL-6, and TNFα) nor an increase in markers of liver or kidney injury [aminotransferases, alkaline phosphatase (ALP), and blood urea nitrogen (BUN); fig. S21].

The superior antitumor efficacy of combination therapy mediated by T-Tre/BCN-Lipo-Ava cells was further confirmed in a second tumor model via intradermal injection of ovalbumin (OVA)–expressing B16F10 melanoma cells (B16F10-OVA) into wild-type

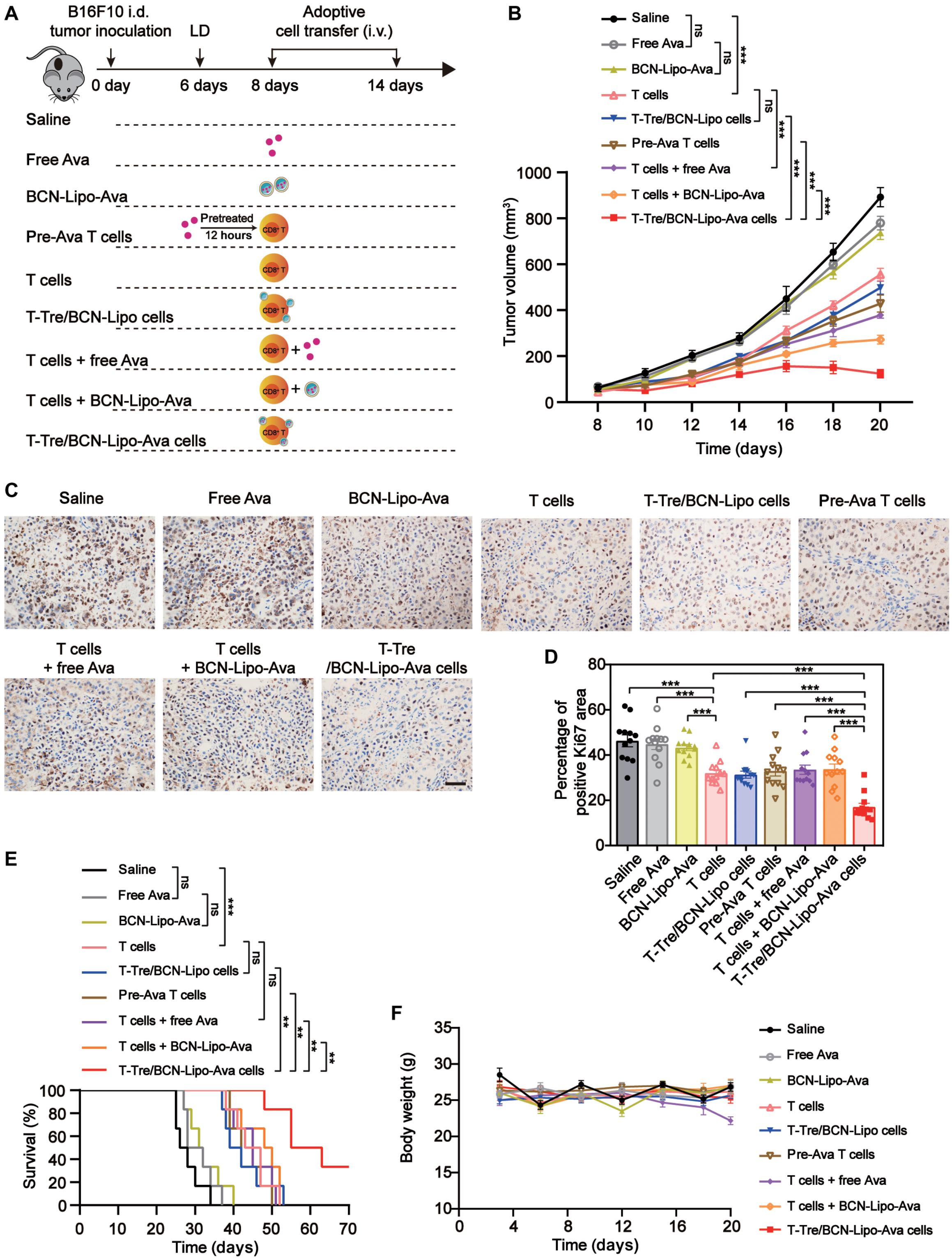

Fig. 4. Antitumor efficacy of pmel-1 CD8$^+$ T-Tre/BCN-Lipo-Ava cells in an orthotopic melanoma mouse model. (**A**) Schematic illustration of the experimental design. i.d., intradermally; i.v., intravenously. (**B**) Tumor growth curves of mice receiving each treatment ($n = 6$ mice per group). (**C**) Representative microscopic images and (**D**) quantification of tumor sections immunostained for Ki67 and the Ki67-positive areas quantified for each field ($N = 12$). Scale bar, 50 μm. (**E**) Survival curves of mice receiving each treatment ($n = 6$ mice per group). (**F**) Body weights of all mice ($n = 6$ mice per group). Error bars denote SEM. Data were analyzed by one-way ANOVA with Tukey's correction (B and C) or a log-rank (Mantel-Cox) test (E). Error bars denote SEM. *$P < 0.05$, **$P < 0.01$, ***$P < 0.001$. ns denotes no significant difference.

C57BL/6 mice and treatment with OVA-specific OT-I CD8$^+$ T-Tre/BCN-Lipo-Ava cells (fig. S22A). The measurement of tumor growth curves, survival curves, and body weights of tumor-bearing mice, as well as the immunohistochemistry of Ki67 staining in tumor sections, were performed as in the B16F10 model. Treatment with OT-I CD8$^+$ T-Tre/BCN-Lipo-Ava cells exhibited the best antitumor efficacy, resulting in markedly delayed tumor growth and improved survival (fig. S22, B to E). As before, body weight, systemic cytokine release, and liver/kidney injury markers were comparable with other groups (figs. S22F and S23). These results therefore indicated that T-Tre/BCN-Lipo-Ava cell therapy afforded improved treatment benefits against primary solid tumors in vivo compared with monotherapies and with the combination treatment of T cells and free Ava.

Antitumor responses of adoptively transferred and tumor-infiltrating CD8$^+$ T cells

We hypothesized that the superior antitumor capacities of T-Tre/BCN-Lipo-Ava cell therapy in vivo stemmed from the enhanced T cell effector functions mediated by modified cholesterol metabolism. To verify this hypothesis, we first isolated adoptively transferred pmel-1 CD8$^+$ T cells from primary melanoma tumors on day 12 after inoculation (4 days after first treatment) and investigated their capacity to secrete inflammatory cytokines, including IFNγ, TNFα, and lytic enzyme granzyme B (GzmB). As displayed in Fig. 5 (A and B), intravenous injection of pre-Ava T cell slightly increased the percentage of IFNγ$^+$, TNFα$^+$, and GzmB$^+$ pmel-1 T cells in tumors as compared to that of unmodified T cell–treated mice, which was in agreement with its modest in vitro cytotoxicity and in vivo antitumor efficacy (Figs. 3A and 4B). Mice receiving the combination of pmel-1 T cells and BCN-Lipo-Ava showed an improved percentage of IFNγ$^+$, TNFα$^+$, and GzmB$^+$ pmel-1 T cells (Fig. 5, A and B), presumably due to the moderate effect between T cells and Ava. The transferred T-Tre/BCN-Lipo-Ava cells displayed greatest proportion of cytokine and cytolytic granule positive T cells (Fig. 5, A and B), likely due to the optimized action profile of backpacked Ava. The cholesterol content in the transferred T-Tre/BCN-Lipo-Ava cells was greater compared to the T cells or the mix of T cells with BCN-Lipo-Ava (Fig. 5, C and D). These results suggest that backpacked Ava is required to maintain high and sustained cholesterol content for potent antitumor efficacy.

When mice received combination therapy via pmel-1 T-Tre/BCN-Lipo-Ava cells, total tumor-infiltrating CD8$^+$ T cells exhibited the highest percentage of TNFα$^+$, IFNγ$^+$, and GzmB$^+$ CD8$^+$ T cells (fig. S24, A and B). These cells also exhibited the highest intensity of Ki67 and Filipin III staining compared to other treatment groups (fig. S24, C and D). These results indicate that backpacked Ava acted in a paracrine manner to increase the antitumor effect of endogenous tumor-infiltrating CD8$^+$ T cells. Similarly, mice receiving OT-I CD8$^+$ T-Tre/BCN-Lipo-Ava cells had the largest percentage of cytotoxic CD8$^+$ T cells in their primary melanoma tumors (fig. S25).

Last, we assessed the exhaustion and immunosuppressive status of adoptively transferred pmel-1 T cells according to the expression of different markers for proliferation (Ki67), T cell exhaustion (TIM-3, LAG-3, and TIGIT), and immunosuppression (PD-1 and CTLA-4) in primary melanoma tumors. The results showed that pmel-1 T-Tre/BCN-Lipo-Ava cells and the combination of pmel-1 T cells and BCN-Lipo-Ava resulted in comparable exhaustion and immunosuppressive markers (fig. S26, A and B), whereas Ki67 expression was increased in pmel-1 T-Tre/BCN-Lipo-Ava cells (Fig. 5, C and D). Similar results were observed in total tumor-infiltrating CD8$^+$ T cells when comparing the T-Tre/BCN-Lipo-Ava cells group with other treatment groups (figs. S24, C and D, and S26, C and D). Of note, in the T-Tre/BCN-Lipo-Ava cell treatment group, the backpacked Ava markedly increased cytokine and cytolytic granule production (IFNγ, TNFα, and GzmB) of PD-1$^+$, TIM-3$^+$, and TIGIT$^+$ pmel-1 T cells (Fig. 5, E to G). Together, these results suggest that T-Tre/BCN-Lipo-Ava cells are not in an exhausted state and that backpacked Ava contributes to the effector function of adoptively transferred T-Tre/BCN-Lipo-Ava cells in the tumor microenvironment by increasing their proliferative capacity, cytokine production, and cytolytic granule production.

In vivo T-Tre/BCN-Lipo-Ava cell therapy for disseminated solid tumors

To demonstrate the potential T-Tre/BCN-Lipo-Ava cells to treat solid tumor dissemination, we intravenously injected mice with luciferase-expressing B16F10-OVA. The treatment regimen was identical to that for primary solid tumor, except that the development of tumors was monitored via the bioluminescence of B16F10-OVA cells. We found that mice receiving OT-I CD8$^+$ T-Tre/BCN-Lipo-Ava cells developed the fewest lung and bone tumors compared with mice receiving monotherapies or even the combination therapy without backpacking (Fig. 6A). Moreover, hematoxylin and eosin (H&E) staining of lungs harvested from tumor-bearing mice confirmed that treatment with OT-I CD8$^+$ T-Tre/BCN-Lipo-Ava cells resulted in fewer tumors of smaller sizes (Fig. 6, B and C, and fig. S27). Furthermore, three of five mice receiving OT-I CD8$^+$ T-Tre/BCN-Lipo-Ava cells survived at least 60 days. In contrast, no mice in the monotherapy groups or in the T cell + free Ava group survived after 60 days, and only one mouse in the T cell plus BCN-Lipo-Ava–treated group survived past 60 days (Fig. 6D). The adoptive transfer of OT-I CD8$^+$ T-Tre/BCN-Lipo-Ava cells did not provoke overt systemic inflammation or cause loss of body weight or detectable damage to major organs including liver, kidney, and spleen (Fig. 6E and fig. S28). Last, we analyzed the production of cytokines and cytolytic granule release of tumor-infiltrating CD8$^+$ T cells. Consistent with the results observed in primary melanoma (figs. S24 and S25), the largest percentages of IFNγ$^+$, TNFα$^+$, and GzmB$^+$ producing CD8$^+$ T cells in pulmonary melanoma were isolated from mice receiving OT-I CD8$^+$ T-Tre/BCN-Lipo-Ava cells (fig. S29).

In vivo T-Tre/BCN-Lipo-Ava cell therapy for aggressive brain tumors

Encouraged by the promising antitumor effect of T-Tre/BCN-Lipo-Ava cell therapy, we extended its application into the treatment of an orthotopic mouse model of an aggressive human glioblastoma, LN-229, which expresses a disialoganglioside, GD-2 (fig. S30). To this end, we first generated and characterized GD-2–specific CAR T cells (fig. S31) according to previous reports (*43*). We generated CAR T-Tre/BCN-Lipo-Ava cells following the same procedures used to generate the pmel-1 T-Tre/BCN-Lipo-Ava cells (fig. S32). LN-229 tumor–bearing mice were treated with combinations of GD-2–specific CAR T cells 6 and 12 days after tumor implantation (Fig. 7A). Using bioluminescence imaging, we found that mice receiving T-Tre/BCN-Lipo-Ava cells could control tumor growth, with three of five mice showing no detectable tumor (Fig. 7B). Mice treated with a combination of CAR T cells and BCN-Lipo-Ava

(T cells + BCN-Lipo-Ava) displayed delayed, but not prevented, tumor growth. The antitumor capacities of monotherapies, including free Ava and CAR T cells, were limited (Fig. 7B). Three of five mice receiving T-Tre/BCN-Lipo-Ava cells survived to 100 days, but mice from all other groups survived no more than 70 days, as presented in Fig. 7C. We observed no obvious loss of body weight (Fig. 7D), nor obviously evaluated systemic cytokine concentrations (Fig. 7, E to G) in mice receiving T-Tre/BCN-Lipo-Ava cells. Together, these findings indicate that T-Tre/BCN-Lipo-Ava cell therapy is safe and effective against intracranial LN-229 tumors.

DISCUSSION

It is increasingly being recognized that T cells undergo metabolic exhaustion in the oxygen- and nutrient-limited tumor microenvironment, which may largely contribute to the failure of T cell therapies against solid tumors (*11*). Zhang and Romero (*44*) suggested that there are three strategies to improve T cell therapies against solid tumors via metabolic interventions. The first recommended intervention is preconditioning T cells with metabolic modulators during in vitro expansion for adoptive T cell therapy (*45*–*47*). However, the in vitro reprogrammed T cell metabolism may be reversed within the tumor microenvironment (*48*). A second strategy is systemic administration of free metabolic modulators. This approach is limited because of its nonspecific distribution and the poor pharmacokinetic profile of these compounds (*49*, *50*). The third option is targeted delivery of metabolic modulators into the tumor microenvironment using nanoparticles or oncolytic viruses. However, delivering the compounds into cells of interest, such as T cells, is challenging because the harsh microenvironment of solid tumors can restrict the entry of compounds into specific cells (*51*). We decided to draw from the strong points of each strategy to develop a combination of metabolic interventions and T cell therapy via cell-surface anchor-engineering (T-Tre/BCN-Lipo-Ava cell) with the goal of boosting solid tumor immunotherapy. T-Tre/BCN-Lipo-Ava cells yielded improved T cell metabolic fitness within the

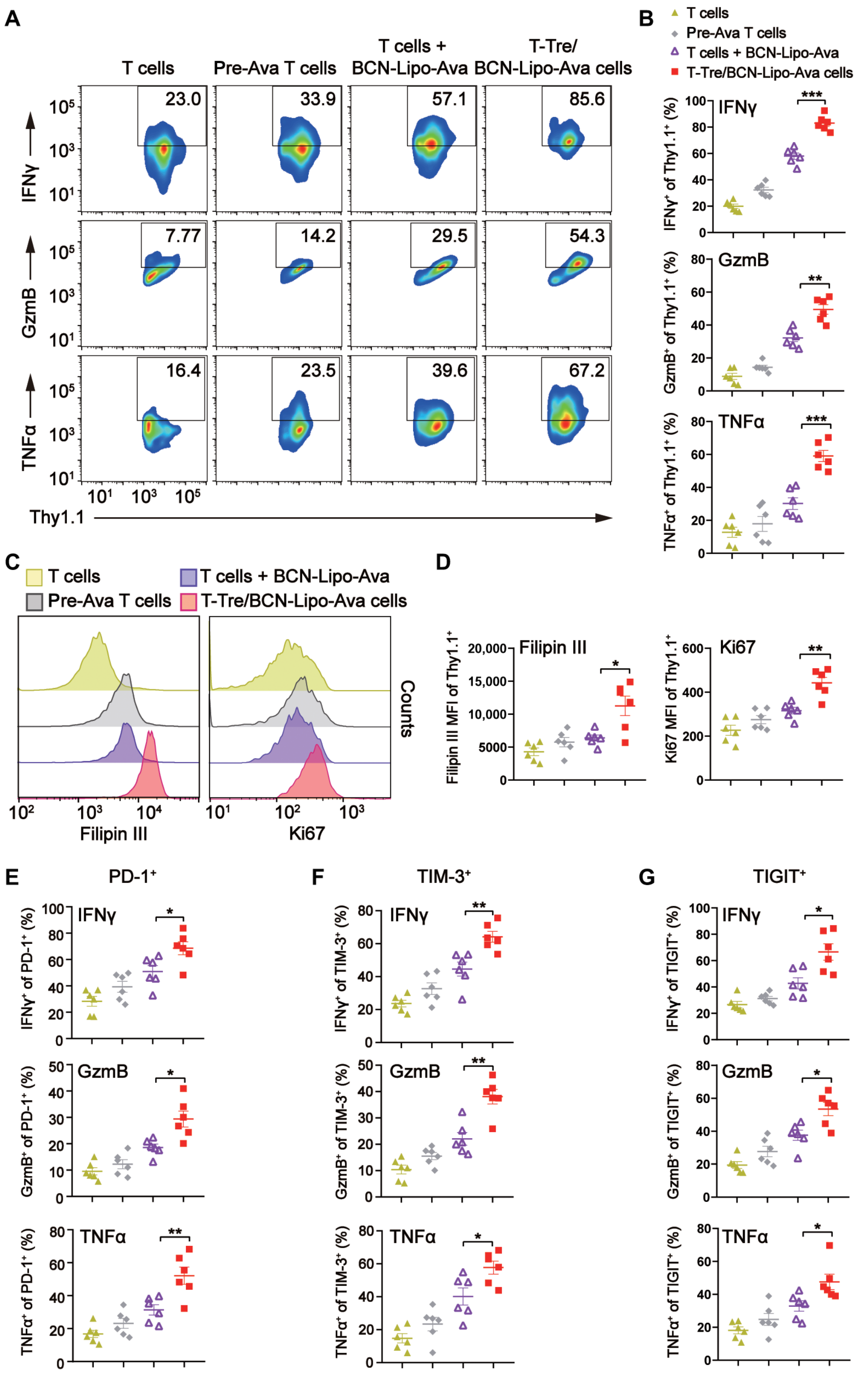

Fig. 5. Antitumor responses, exhaustion, and proliferation of tumor-infiltrating pmel-1 CD8$^+$ T cells in flank B16F10 tumors after a single adoptive transfer. (**A**) Flow cytometry analysis and (**B**) quantification of intracellular TNFα, IFNγ, and GzmB in pmel-1 T cells isolated from orthotopic B16F10 melanoma tumors after injection of Thy1.1$^+$ pmel-1 T cells for 4 days ($n = 6$ mice per group). (**C**) Filipin III and (**D**) Ki67 content of tumor-infiltrating transferred Thy1.1$^+$ pmel-1 T cells were assessed using flow cytometry ($n = 6$ mice per group). Flow cytometry analysis of (**E**) TNFα, (**F**) IFNγ, and (**G**) GzmB in PD-1$^+$, TIM-3$^+$, or TIGIT$^+$ Thy1.1$^+$ pmel-1 T cells in orthotopic melanoma tumors ($n = 6$ mice per group). Data were analyzed by one-way ANOVA test with Tukey's correction. Error bars denote SEM. $^*P < 0.05$, $^{**}P < 0.01$, $^{***}P < 0.001$. ns denotes no significant difference.

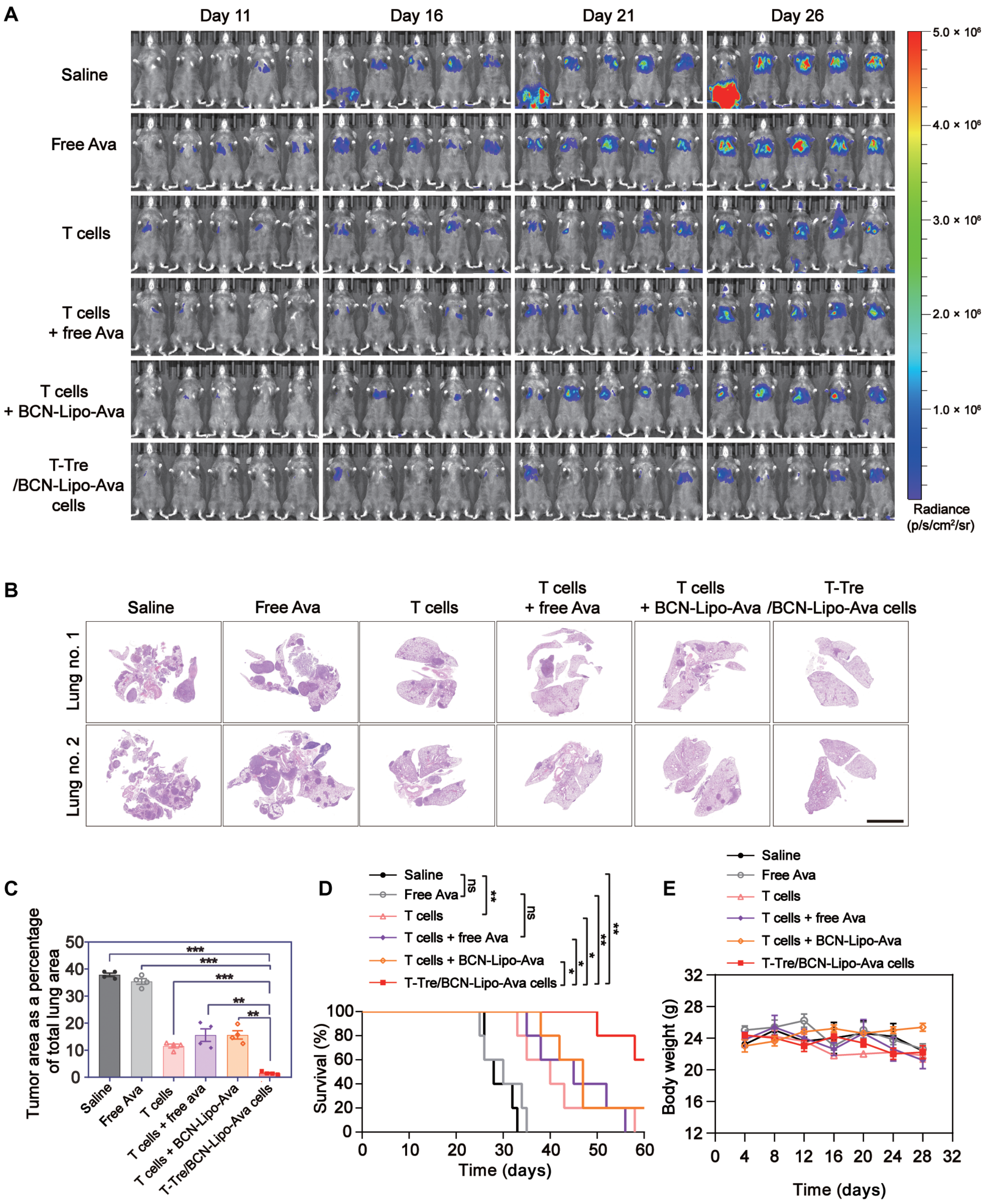

Fig. 6. Enhanced efficacy of OT-I CD8$^+$ T-Tre/BCN-Lipo-Ava cells in an experimental disseminated melanoma mouse model. (**A**) In vivo bioluminescence images of mice bearing melanoma tumors in the lungs ($n = 5$ mice per group). (**B**) Representative microscopic hematoxylin and eosin–stained images (sale bar, 5 mm) and (**C**) quantification of lung sections harvested from mice receiving each treatment on day 30. Whole lung sections were imaged, and tumor area was quantified ($n = 4$ mice per group). (**D**) Survival curves of mice receiving each treatment ($n = 5$ mice per group). (**E**) Body weights of all mice ($n = 5$ mice per group). Data were analyzed by one-way ANOVA with Tukey's correction (C) or a log-rank (Mantel-Cox) test (D). Error bars denote SEM. $^*P < 0.05$, $^{**}P < 0.01$, $^{***}P < 0.001$. ns denotes no significant difference.

tumor microenvironment by a sustained and prolonged release of Ava. In addition, retaining Ava on the T cell surface afforded an autocrine- and paracrine-like mechanism of action for Ava, which was critical for optimal efficacy (*23*).

Although T-Tre/BCN-Lipo-Ava cells demonstrated no overt toxicity in our animal studies, the long-term toxicity should be thoroughly investigated before translation into the clinic. To this end, clinically approved metabolic-modulating drugs can be investigated

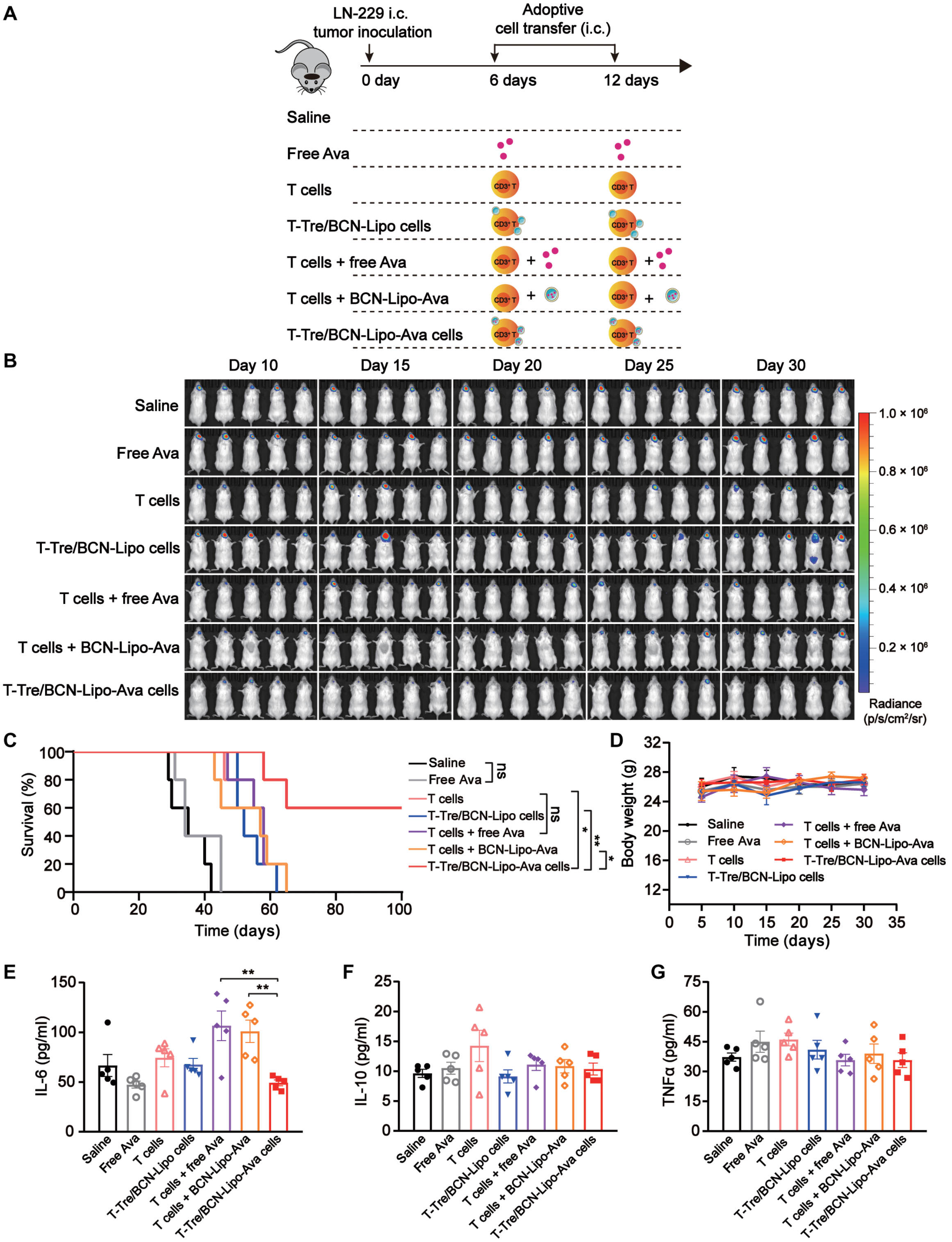

Fig. 7. Adoptive CAR T-Tre/BCN-Lipo-Ava cell transfer promoted survival in an orthotopic glioblastoma mouse model. (**A**) Schematic illustration of the experimental design. i.c., intracranial. (**B**) In vivo bioluminescence images of mice bearing glioblastoma tumors ($n = 5$ mice per group). (**C**) Survival curves of mice receiving each treatment ($n = 5$ mice per group). (**D**) Body weights of all mice ($n = 5$ mice per group). Serum (**E**) IL-6, (**F**) IL-10, and (**G**) TNFα concentrations as measured by ELISA ($n = 5$ mice per group). Data were analyzed by one-way ANOVA with Tukey's correction (E) or a log-rank (Mantel-Cox) test (C). Error bars denote SEM. $^*P < 0.05$, $^{**}P < 0.01$, $^{***}P < 0.001$. ns denotes no significant difference.

for use in cell-surface anchor-engineering. Further investigation, including the improvement of the physical stability of liposomes by optimizing lipid compositions, will be necessary to increase the therapeutic window of combined drugs. An additional limitation of this study is the use of adoptive T cell therapy, which requires a lengthy manufacturing process for patients and may result in graft-versus-host disease, cytokine release syndrome, or neurotoxicity. To overcome this limitation, the anchor-engineering strategy presented here could be applied to other types of cells, such as natural killer cells and neutrophils.

In conclusion, this rational combination of metabolic intervention and T cell therapy yielded improved efficacy in two murine tumor models and provided an alternative combination strategy for boosting solid tumor immunotherapy. In addition, this study serves as a proof of concept for cell-surface anchor-engineering, which can be easily tailored to other combinations of cell therapy and clinically approved metabolic drugs and/or antibodies. Last, this cell-surface anchor-engineering expands the range of nongenetic T cell engineering strategies and can be deployed to various cell types.

MATERIALS AND METHODS

Study design

This study was designed to investigate a combination of metabolic reprogramming and T cell therapy via surface anchor-engineering to improve efficacy of immunotherapy in solid tumors. To investigate the antitumor efficacy of T-Tre/BCN-Lipo-Ava cells, we designed a series of in vitro and in vivo experiments. For in vivo experiments, animals were randomly assigned into treatment groups. The sample size was determined by previous experience and preliminary experiments. All mice were included in our analysis if a tumor was established. Sample sizes are denoted in figures or figure legends and refer to number of animals unless stated otherwise. The determination of treatment efficacy was assessed by the tumor size, whole-body luciferase imaging, and survival time of mice, as well as the representative markers of T cells. The body weight changes, histopathological changes, and inflammatory responses in mice were investigated to evaluate safety. For confocal imaging, the image acquisition and analysis were performed blinded. All results shown are either representative of or mean of at least three independent samples (otherwise annotated in the legends).

Cell lines and mice

The human glioblastoma cell line LN-229, the human prostatic carcinoma cell line PC-3, and the mouse melanoma cell line B16F10 were all purchased from the American Type Culture Collection. LN-229 cells were cultured in Dulbecco's modified Eagle's medium (DMEM) with 5% FBS and 1% penicillin-streptomycin. PC-3 cells were cultured in DMEM-F12 with 10% FBS and 1% penicillin-streptomycin. B16F10 cells were cultured in DMEM with 10% FBS and 1% penicillin-streptomycin. B16F10 cells were stably transfected with the plasmid pAc-neo-OVA (B16F10-OVA) that carried chicken OVA mRNA by electroporation using Gene Pulser Xcell (Bio-Rad Laboratories). For bioluminescent in vivo tumor imaging, we transduced the B16F10-OVA and LN-229 cells with a firefly luciferase–expressing lentivirus (GeneChem) according to the manufacturer's instructions. Human CD3$^+$ pan T cells were purchased from Miao Tong Biological Technology Co. Ltd. Nonobese diabetic/severe combined immunodeficient/IL2R$\gamma^{-/-}$ (NSG; 18 to 20 g, male) mice and TCR transgenic OT-I mice (18 to 20 g, male) were purchased from GemPharmatech Co. Ltd. TCR transgenic Thy1.1$^+$ pmel-1 mice were purchased from The Jackson Laboratory. C57BL/6J mice (18 to 20 g, male) were obtained from Beijing Vital River Laboratory Animal Technology Co. Ltd. All animals were pathogen free and allowed access to food and water freely. The Animal Care and Use Committee of the China Pharmaceutical University approved all of the animal studies and animal protocols.

Chemistry

Detailed synthesis method of each compound is listed in the Supplementary Materials. To successfully modify the cell surface by click reaction, a cyclononynyl-derivatized phospholipid analog (DSPE-BCN) was synthesized as a lipid click module, and a tetrazinyl-derivatized PEG phospholipid analog (DSPE-PEG$_{5k}$-Tre) was synthesized for the insertion of cell membrane. Two fluorescently labeled tetrazine derivatives (FITC-DSPE-PEG$_{5k}$-Tre and DSPE-PEG$_{5k}$-FITC) were also synthesized for fluorescence imaging. All above structures were confirmed by ^{1}H-NMR, and DSPE-BCN was also confirmed by MS. Ultraviolet spectroscopy was performed to detect the reaction between the two modules at 540 nm.

Isolation of mouse CD8$^+$ T cells

Spleens from C57BL/6J Thy1.1$^+$ pmel-1 mice or C57BL/6J OT-I mice were ground through a 70-μm filter, and red blood cells were removed by incubation with ACK lysis buffer for 5 min at 4°C. Then, the splenic cells were centrifuged, washed with D-PBS (without Ca^{2+} and Mg^{2+}), and isolated by the EasySep Mouse CD8+ T Cell Isolation Kit (StemCell) to obtain naive pmel-1 Thy1.1$^+$ CD8$^+$ T cells (pmel-1 CD8$^+$ T cells) or OT-I CD8$^+$ T cells. To activate CD8$^+$ T cells, naive CD8$^+$ T cells were resuspended at 1.5 × 10^6 cells/ml in RPMI medium containing recombinant mouse IL-2 (10 ng/ml), plate-bound anti-CD3 (5 μg/ml), and anti-CD28 agonist antibodies (2 μg/ml) and incubated at 37°C. After an incubation period of 2 days, dead cells were removed by centrifugation, and living cells were collected. Activated CD8$^+$ T cells were cultured in medium containing IL-2 and anti-CD3 and anti-CD28 agonist antibodies for in vitro and in vivo studies.

Preparation and characterization of T-Tre/BCN-Lipo-Ava cells

T-Tre/BCN-Lipo-Ava cells were obtained by incubating CD8$^+$ T cells sequentially with DSPE-PEG$_{5K}$-Tre and BCN-Lipo-Ava. Briefly, CD8$^+$ T cells (1 × 10^6 cells/ml) were resuspended in serum-free medium. Then, CD8$^+$ T cells were incubated with DSPE-PEG$_{5K}$-Tre (80 μg/ml) at 37°C for 10 min. After two washes with ice-cold PBS, cells were incubated with BCN-Lipo-Ava with Ava at 100 μg/ml at 37°C for 30 min. The CD8$^+$ T cells with surface-anchored BCN-Lipo-Ava were collected by centrifugation at 800*g* for 5 min, washed with PBS, and resuspended in medium for in vitro or in vivo studies. The concentration of Ava in T-Tre/BCN-Lipo-Ava cells was determined using HPLC (HPLC-LC-2010A HT, Shimadzu). CAR T-Tre/BCN-Lipo-Ava cells were prepared using the same method.

For the preparation of T cells anchored with fluorescent liposomes, CD8$^+$ T cells (1 × 10^6 cells/ml) were incubated with FITC-DSPE-PEG$_{5K}$-Tre, FITC-DSPE-PEG$_{5K}$, or DSPE-PEG$_{5K}$-Tre (80 μg/ml) at 37°C for 10 min. After washing with PBS, BCN-Lipo-RhoB or RhoB-Lipo was incubated with cells at 37°C for 30 min. After washing with PBS, the CD8$^+$ T cells anchored with fluorescent anchoring modules or fluorescent liposomes were stained with Hoechst 33342, fixed with 4% paraformaldehyde (PFA), and used immediately for confocal imaging and flow cytometry analysis.

To further confirm that our surface anchor-engineering strategy enabled the anchoring of nanoparticles on the T cell surface, we obtained BCN-modified Au nanoparticles (BCN-Au) through BCN-PEG-SH reaction with Au nanoparticles. Then, the CD8$^+$ T cells were incubated with DSPE-PEG$_{5K}$-Tre for 10 min. After washing with PBS, cells were further incubated with BCN-Au at 37°C for 30 min. CD8$^+$ T cells with surface-anchored Au nanoparticles were collected by centrifugation at 800*g* for 5 min. The cells were fixed with 2.5% glutaraldehyde aqueous solution overnight. After washing with PBS three times, samples were dehydrated with gradient ethanol and imaged by SEM (Quanta 250, FEI).

To investigate the stability of liposomes on the surface of T cells, RhoB-labeled T-Tre/BCN-Lipo-Ava cells were cultured and expanded for 2 and 4 days. Then, the cells were collected, stained with Hoechst 33342, and fixed with 4% PFA for confocal imaging and flow cytometry analysis. To further assess drug stability on T-Tre/BCN-Lipo-Ava cells, we determined the amounts of Ava in the supernatant, intracellular compartment, and filtered compartment using HPLC. The in vitro stability of T-Tre/BCN-Lipo-Ava cells was evaluated under different conditions, including normal physiological condition (PBS, pH 7.4) and FBS. Briefly, T-Tre/BCN-Lipo-Ava cells (1 × 10^6 cells per well) were seeded in 24-well plates and then incubated with RPMI 1640 medium or 50% FBS in RPMI 1640 medium for different periods (0, 2, 4, 6, 8, 10, 12, 24, 48, and 72 hours). The amounts of Ava anchored on T-Tre/BCN-Lipo-Ava cells and released into the supernatant medium were determined using HPLC.

To calculate the number of liposomes anchored on the surface of T cells, 1 × 10^6 CD8$^+$ T cells were first incubated with DSPE-PEG$_{5k}$-Tre or DSPE-PEG$_{5k}$ (80 μg/ml) at 37°C for 10 min. After washing with PBS twice, T cells were then incubated with the BCN-Lipo-Ava solution in 1 ml for 30 min. The concentration of BCN-Lipo-Ava in the solution was assessed with Nanoparticle Tracking Analyzer (Malvern NanoSight NS300). The liposome number anchored on the surface of CD8$^+$ T cells per million was calculated as follows: $(n_{\text{before DSPE-PEG-Tre}} - n_{\text{after DSPE-PEG-Tre}}) - (n_{\text{before DSPE-PEG}} - n_{\text{after DSPE-PEG}})/10^6$, where $n_{\text{before DSPE-PEG-Tre}}$ and $n_{\text{before DSPE-PEG}}$ were the counted numbers of liposomes in the solution before the incubation of BCN-Lipo-Ava with T cells, and $n_{\text{after DSPE-PEG-Tre}}$ and $n_{\text{after DSPE-PEG}}$ were the counted numbers of liposomes in the supernatant after the incubation of BCN-Lipo-Ava with T cells. The counts of $n_{\text{before DSPE-PEG}}$ minus $n_{\text{after DSPE-PEG}}$ were used to calculate nonspecific adsorption of liposomes on the surface of T cells.

Evaluation of physiological functions of T-Tre/BCN-Lipo-Ava cells

The physiological functions of T-Tre/BCN-Lipo-Ava cells were evaluated, including viability, apoptosis, proliferation, chemotaxis, and activation. For viability analysis, 1 × 10^6 T cells and T-Tre/BCN-Lipo-Ava cells were cultured in RPMI 1640 medium containing recombinant mouse IL-2 (10 ng/ml), plate-bound anti-CD3 (5 μg/ml), and anti-CD28 agonist antibodies (2 μg/ml). On days 0, 3, 6, 8, and 10, the cells were collected for trypan blue staining and cell counting to calculate the survival rate of the cells. Meanwhile, 1 × 10^6 T cells were incubated with RPMI 1640 medium without anti-CD3 and anti-CD28 antibodies as control. Survival rate (%) = number of unstained cells/total number of cells × 100%.

For the apoptosis analysis, 1 × 10^6 T cells and T-Tre/BCN-Lipo-Ava cells were stimulated by plate-bound anti-CD3 (5 μg/ml) and anti-CD28 agonist antibodies (2 μg/ml) for 10 days and were collected and suspended in 0.5 ml of 1× binding buffer and washed twice with ice-cold PBS. The Annexin V-FITC Apoptosis Detection Kit (Vazyme) was used according to the manufacturer's instructions for the apoptosis assay. The stained cells were analyzed with an Attune NxT flow cytometer (Thermo Fisher Scientific).

For the proliferation assay, T cells and T-Tre/BCN-Lipo-Ava cells were resuspended at 1 × 10^7/ml in prewarmed serum-free RPMI 1640 medium. CFSE was added to the cells at a final concentration of 2 μM, and cells were incubated at 37°C for 15 min. CFSE staining was quenched by adding a 1:1 volume ratio of cold RPMI 1640 medium with 10% FBS, and cells were centrifuged at 500*g* for 3 min followed by two more washes in cold RPMI with FBS. Then, the cells were resuspended in RPMI medium containing IL-2, and anti-CD3/CD28 beads (Dynabeads Mouse T-Activator CD3/CD28) were added to the medium at a bead-to-cell ratio of 1:1. Two days after activation, T cells were mixed with counting beads, washed once with fluorescence-activated cell sorting (FACS) buffer, and then returned to the incubator. At days 3 and 5, the cells were collected and washed with PBS before analysis by flow cytometry. To further measure proliferation, T cells and T-Tre/BCN-Lipo-Ava cells were cultured in RPMI 1640 medium containing recombinant mouse IL-2 (10 ng/ml) in culture plates precoated with anti-CD3 (5 μg/ml) and anti-CD28 (2 μg/ml) agonist antibodies. At days 0, 3, 6, 8, and 10, the cells were collected and counted. Fold expansion rate (%) = number of cells/number of cells (day 0) × 100%.

To measure the transvascular migration capacity of surface anchor-engineered T cells, we established a transwell model with a confluent endothelial [human umbilical cord endothelial cells (HUVECs)] monolayer. Briefly, HUVECs (2 × 10^5 cells per well) were seeded onto the upper chamber of the transwell (3 μm, 24 mm) and cultured with medium containing FBS (10% v:v). The integrity of the cell monolayer was evaluated by measuring the transepithelial electrical resistance (TEER) values using a Millicell-ERS voltohmmeter (Millipore). Cell monolayers with TEER value higher than 300 ohm·cm^2 were used for the transmigration studies. T-Tre/BCN-Lipo-Ava cells (1.25 × 10^6) were added to the upper chamber with TNFα (25 ng/ml) for 4 hours, and MCP-1 (20 ng/ml) was added into the lower chamber to induce the migration. After 12 hours of incubation, the supernatant in the upper chamber and the medium in the lower chamber were sampled, and the HUVEC cell layers on the membrane of the transwell were harvested. The amount of Ava in the supernatant, intracellular compartment, and filtered compartment was determined using HPLC. The Ava ratio in each compartment was calculated compared with the initial amount of Ava. The number of T cells in the lower chamber was also counted.

The chemotaxis of T-Tre/BCN-Lipo-Ava cells was investigated using a transwell migration assay (Corning). Briefly, 1 × 10^6 T-Tre/BCN-Lipo-Ava cells or unmodified CD8$^+$ T cells were added to the upper chamber of the transwell, and different concentrations of MCP-1 (5, 20, and 100 ng/ml) were added into the lower chamber to induce the migration. After 12 hours of incubation, the cells in the lower chamber were harvested and the numbers were counted using a hemocytometer. The chemotaxis index $((n_{\text{T-Tre/BCN-Lipo-Ava}} - n_{\text{control}})/n_{\text{control}})$ was calculated, where $n_{\text{T-Tre/BCN-Lipo-Ava}}$ and n_{control}

are the counted numbers of CD8$^+$ T cells in the lower chamber after incubating with T-Tre/BCN-Lipo-Ava cells in the presence of MCP-1 and the unmodified CD8$^+$ T cells in the absence of MCP-1, respectively.

To verify the activation status of T-Tre/BCN-Lipo-Ava cells, naive unmodified T cells and T-Tre/BCN-Lipo-Ava cells were plated on 96-well microtiter plates and stimulated with anti-CD3/CD28 agonist antibody beads (Dynabeads Mouse T-Activator CD3/CD28). After 24-hour incubation, the cells were collected and stained with FITC anti-mouse CD69 antibody (BioLegend), and expression of the early T cell activation marker CD69 was quantified by flow cytometry.

In addition, CD8$^+$ T cells were stimulated with ConA (Sigma-Aldrich) in different concentrations for 2 days and rested for another 1 day. Then, cells were anchored with BCN-Lipo-Ava or incubated with 1 μM free Ava for 24 or 48 hours. The cell supernatant was used to measure IL-2, TNFα, and IFNγ production in CD8$^+$ T cells by enzyme-linked immunosorbent assay (ELISA) (Elabscience) according to the instruction of the manufacturer.

Measurement of CD8$^+$ T cell cytotoxicity

To measure CD8$^+$ T cell cytotoxicity, activated pmel-1 CD8$^+$ T cells, Ava-pretreated pmel-1 CD8$^+$ T cells, and pmel-1 CD8$^+$ T-Tre/BCN-Lipo-Ava cells were washed three times with PBS and then mixed with B16F10 (1×10^5) in phenol-free RPMI 1640, 2% FBS at the ratio of 10:1. After 4, 12, and 24 hours, the cytotoxic efficiency was measured by quantifying the release of endogenous lactate dehydrogenase (LDH) from B16F10 cells using the LDH Cytotoxicity Assay Kit (Beyotime Biotechnology) according to the instruction of the manufacturer.

Super-resolution STED imaging

The confocal chamber was first treated with 0.01% (w/v) poly-L-lysine solution for 2 hours. The solution was then discarded, and the confocal chamber was placed at room temperature for 15 min to dry. Next, anti-mouse CD3 antibody (20 μg/ml) was added into the chamber and incubated overnight at 4°C. After the incubation, the chamber was washed once with PBS. Meanwhile, 1×10^6 T-Tre/BCN-Lipo-Ava cells or 1×10^6 CD8$^+$ T cells were cultured for 12 hours, and another group of 1×10^6 CD8$^+$ T cells was added to 1 μM free Ava for 12 hours. The cells were plated in pretreated confocal chambers, incubated at 37°C for 10 min, and fixed with 4% PFA for 15 min at room temperature. After two washes with PBS, CD8$^+$ T cells were incubated with Alexa Fluor 647 anti-mouse TCR β-chain antibody (2 μg/ml; BioLegend) for 20 min at room temperature and again washed twice with PBS. Afterward, the cells were incubated with 0.2% Triton X-100 for 10 min, washed with PBS, and blocked with nonspecific binding protein for 30 min at room temperature with 2% bovine serum albumin. Alexa Fluor 488 anti-ZAP70 Phospho (Tyr^{319})/Syk Phospho (Tyr^{352}) antibody (2 μg/ml; BioLegend) was added to cells, and cells were incubated for 1 hour at room temperature. The abundance of TCR and phosphorylated ZAP70 on the membrane of CD8$^+$ T cells was imaged by stimulated emission depletion (STED) microscopy (Leica TCS SP8). Super-resolution STED images were analyzed using Leica LAS X.

Western blotting

To assess the effect of Ava on TCR signaling of CD8$^+$ T cells, CD8$^+$ T cells plus 1 μM free Ava (T cell + free Ava) or CD8$^+$ T cells engineered with Ava-loaded liposomes (T-Tre/BCN-Lipo-Ava cell) were incubated for 12 hours and then stimulated with CD3/CD28 antibodies for different amounts of time (0, 15, or 30 min). The whole-cell protein extracts were isolated using radioimmunoprecipitation assay lysis buffer. Protein concentration was determined by the BCA Protein Assay Kit (Keygen Biotech). About 30 μg of total protein was loaded, fractionated by SDS–polyacrylamide gel electrophoresis, transferred to polyvinylidene difluoride membrane, and probed with anti–β-actin (Absin), anti-pCD3ζ (Tyr^{142}) (Thermo Fisher Scientific), anti-CD3ζ (Bioworld), anti-pZAP70 (Tyr^{319}) (Cell Signaling Technology), anti-ZAP70 (Bioworld), anti-pERK1/2 (Cell Signaling Technology), or anti-ERK1/2 (Cell Signaling Technology). Signal was detected using a chemiluminescence imaging system (Tanon). Band intensities were quantified by densitometric analysis using ImageJ software (Fiji, 1.51n). Each protein band was quantified using the integrated density value (mean pixel density × area).

Super-resolution imaging

CD8$^+$ T cells cultured without Ava for 12 hours, CD8$^+$ T cells incubated with 1 μM free Ava for 12 hours, and T-Tre/BCN-Lipo-Ava cells cultured for 12 hours were set up for imaging of TCR distribution in the plasma membrane using stochastic optical reconstruction microscopy (STORM). T cells were placed in a 35-mm confocal chamber and fixed with 4% PFA, followed by surface staining with anti-TCRα/β (5 μg/ml; Abcam) for 4 hours at 4°C, and then the cells were stained with Alexa Fluor 647–conjugated goat anti-hamster immunoglobulin G (IgG) (2 μg/ml) for 2 hours at 4°C after washing with PBS 10 times. Before imaging, the buffer in the dish was replaced with imaging buffer containing 100 mM β-mercaptoethanolamine (MEA) to enhance fluorescence signal. We analyzed the molecule distribution of super-resolution STORM images with the N-STORM analysis module of NIS-Elements 5.0 (Nikon) based on Ripley's K-function. Ripley's K-function is used to compare a given distribution with a random distribution (*52*, *53*). The equation is as follows: $K(r) = \frac{1}{n}\sum_{i=1}^{n} N_{p_i}(r)/\lambda$. Here, r represents cluster radius, λ means the number of points per area (region of interest), p_i is the ith point, and the sum is taken over n points. The expected value of $K(r)$ for a random Poisson distribution is πr^2, and deviations from the expectation indicate scales of clustering. Then, the K-function is linearly normalized to L-function so that the expected value is r: $L(r) = \sqrt{K(r)/\pi}$. The K-function can be normalized so that the expected value is 0, yielding the so-called H-function: $H(r) = L(r) - r$. $L(r) - r$ represents the efficiency of molecule clustering, whereas the r value at the maximum $L(r) - r$ value represents the cluster size with the highest probability.

Imaging of TCR clustering by TIRFM

Planar lipid bilayers (PLBs) containing biotinylated liposomes were prepared for imaging of TCR clustering. Biotinylated liposomes were prepared by ultrasound treatment of 1,2-dioleoyl-*sn*-glycero-3-phosphocholine (DOPC) (A.V.T. Shanghai Pharmaceuticals Co. Ltd.) and 1,2-dioleoyl-*sn*-glycero-3-phosphoethanolamine-cap-biotin (biotin-DOPC) (Sigma-Aldrich) at a molar ratio of 25:1 in PBS at a total lipid concentration of 5 mM. PLBs were formed in confocal chambers, and 0.1 mM biotinylated-containing PLBs were washed with PBS for 20 min. After washing with PBS, PLBs were incubated with 20 nM streptavidin for 20 min, and residual streptavidin was removed by washing with PBS. Streptavidin-containing PLBs were incubated with 20 nM biotinylated anti-mouse CD3 antibody (17A2)

(BioLegend), and unconjugated antibody was removed by washing with PBS. Last, PLBs were treated with PBS containing 5% FBS for 30 min at 37°C and washed thoroughly. Three groups of cells were set up for the imaging of TCR clustering by total internal reflection fluorescence microscopy (TIRFM): $CD8^+$ T cells cultured without Ava for 12 hours, $CD8^+$ T cells incubated with 1 μM free Ava for 12 hours, and T-Tre/BCN-Lipo-Ava cells cultured for 12 hours. Then, the T cells were stained with anti-mTCRα/β (5 μg/ml; Abcam) and Alexa Fluor 647–conjugated goat anti-hamster IgG (2 μg/ml). TIRFM imaging was performed on a Leica DMI8 microscope. Images were analyzed with ImageJ (Fiji, 1.51n).

Cholesterol quantification

Two methods were used to quantify the cholesterol on T cells. For Filipin III staining, T-Tre/BCN-Lipo-Ava cells were cultured for 12 hours and the CM was collected. Naive and activated cells were incubated with each type of CM for 12 hours. Cells were collected, plated in confocal chambers after centrifugation, and fixed with 4% PFA for 15 min at room temperature. Then, cells were washed twice with PBS and stained with Filipin III (50 μg/ml; Sigma-Aldrich) for 30 min at 4°C. Images were collected using a Zeiss LSM 880 confocal microscope and analyzed using Zeiss ZEN software. In addition, T-Tre/BCN-Lipo-Ava cells, Ava-pretreated T cells, and unconjugated T cells were incubated at 37°C for 12 hours. After incubation, the cells were collected at 0, 2, 4, 8, 12, and 24 hours and stained with Filipin III (50 μg/ml) to quantify the content of plasma membrane cholesterol of T cells over time by flow cytometry.

For oxidation-based cholesterol quantification, activated $CD8^+$ T cells were incubated with the CM of T-Tre/BCN-Lipo-Ava cells for 12 hours or with an equivalent dose of free Ava for 12 hours as positive control. The plasma membrane was collected as previously reported (*54*, *55*), and the cholesterol was quantified using an Amplex Red cholesterol assay kit (Invitrogen) according to the manufacturer's instructions.

In vivo tumor studies

For evaluation of adoptive surface anchor-engineered pmel-1 $CD8^+$ T cells in an orthotopic melanoma model, B16F10 cells (1.0×10^6) were intradermally injected in the flank of C57BL/6J mice on day 0. The B16F10-bearing mice were lymphodepleted with cyclophosphamide (2 mg/kg) and fludarabine (2 mg/kg) on day 6. Then, the mice were randomly divided into nine groups (six mice per group) and received saline, free Ava (2 mg/kg), BCN-Lipo-Ava (2 mg/kg for Ava), pmel-1 $CD8^+$ T cells (1.0×10^7), pmel-1 $CD8^+$ T cell plus free Ava (1.0×10^7, 2 mg/kg for Ava), pmel-1 $CD8^+$ T-Tre/BCN-Lipo cells (1.0×10^7), Ava pretreated pmel-1 $CD8^+$ T cells (1.0×10^7), pmel-1 $CD8^+$ T cells (1.0×10^7) plus unconjugated BCN-Lipo-Ava (2 mg/kg for Ava), or pmel-1 $CD8^+$ T-Tre/BCN-Lipo-Ava cells (1.0×10^7, 2 mg/kg for Ava) by intravenous injection on days 8 and 14 after tumor inoculation. The tumor size was measured by vernier caliper every 2 days, and the animal survival rate was recorded every day. Tumor size was calculated as $(\text{length} \times \text{width}^2)/2$. Weight was recorded on days 3, 6, 9, 12, 15, 18, and 20. Mice with tumors larger than 20 mm at the longest axis were euthanized for ethical considerations. Heart, liver, spleen, lung, and kidney of the mice were collected and weighed to calculate the organ index.

For evaluation of adoptive surface anchor-engineered T cells in a disseminated pulmonary lung disseminated melanoma model, B16F10-OVA-Luci cells (2.0×10^5) were injected intravenously into C57BL/6J mice, and then mice were randomly divided into six groups of five mice and treated as above on day 6. From day 6, mice were imaged for bioluminescence every 5 days to monitor tumor growth, and the animal survival rate was recorded every day. Mice were euthanized when the body weight loss was greater than 20% of the predosing weight. Heart, liver, spleen, lung, and kidney were collected and weighed to calculate the organ index. Orthotopic melanoma tumors and lungs were dissected, embedded in paraffin, sectioned, and stained with H&E using routine methods. Briefly, samples were harvested and fixed overnight in 4% PFA (dissolved in phosphate buffer solution, pH 7.4) (Sigma-Aldrich) at 4°C. Subsequently, the PFA-fixed tissues were transferred to 70% ethanol, dehydrated, embedded in paraffin (Sigma-Aldrich), divided into sections (5 μm thickness), and stained with H&E. Sections were photographed using dotSlide virtual microscopy (Olympus). Morphometric evaluation was performed, and the geometric characteristics of the tumor tissues were assessed using ImageJ (Fiji, 1.51n). Immunohistochemistry of Ki67 was performed on paraffin sections by using rabbit anti-mouse-Ki67 (1:200; Cell Signaling Technology) and staining with the HRP-DAB SPlink Detection Kit (ZSGB-Bio). The Ki67 staining was imaged with Microscope BX53 (Olympus) and analyzed by ImageJ (Fiji, 1.51n) with the ImmunoRatio 1.0 c plugin.

To generate the intracranial glioma model, human luciferase-expressing glioblastoma cells (LN-229-luci cells) were detached by trypsinization, washed, and resuspended in PBS at a concentration of 5×10^5 cells in 5 μl. NSG mice were anesthetized by isoflurane and fixed in a stereotactic frame. Cells (5×10^5) were injected into the right frontal lobe of NSG mice using a microsyringe as previously described (*56*). The injection coordinates for the orthotopic model were 2 mm lateral from the bregma and 1.5 mm deep from the outer border of the cranium. Mice were randomly divided into five groups of five mice and treated with saline, free Ava (1 mg/kg), CAR T cells (5×10^6), CAR T cells plus free Ava (5×10^6, 1 mg/kg for Ava), CAR T-Tre/BCN-Lipo cells (5×10^6), CAR T cells (5×10^6) plus unconjugated BCN-Lipo-Ava (1 mg/kg for Ava), or CAR T-Tre/BCN-Lipo-Ava cells (5×10^6, 1 mg/kg for Ava) by intracranial injection on days 6 and 12. From day 6, mice were weighed and imaged for bioluminescence every 5 days to monitor the tumor growth, and survival of mice was recorded every day. Mice were euthanized when body weight loss was >20% of the predosing weight. Serum samples from each group of mice were collected at day 18 after tumor inoculation and analyzed for IL-6, IL-10, and TNFα concentrations via ELISA Kit (Elabscience).

Measurement of serum cytokine concentrations and liver enzymes

Serum samples from mice treated as described above were collected at day 18 or day 20 after tumor inoculation and analyzed for concentrations of IL-6, IL-10, and TNFα using the ELISA Kit (Elabscience and Multisciences). The quantities of ALP, alanine transaminase (ALT), aspartate transaminase (AST), BUN, and LDH were determined per kit instructions.

In vivo bioluminescence imaging

Luciferase substrate D-luciferin (Yeasen) suspended in ddH_2O (15 mg/ml) was intraperitoneally injected (150 mg/kg) 10 min before imaging. Bioluminescence images were collected on the IVIS Spectrum Imaging System (PerkinElmer). Living Image software (PerkinElmer) was used to acquire and quantify the bioluminescence imaging datasets.

Phenotyping of adoptively transferred and endogenous tumor-infiltrating CD8$^+$ T cells in the B16F10 orthotopic melanoma model

After injection of pmel-1 CD8$^+$ T-Tre/BCN-Lipo-Ava cells into B16F10-bearing mice for 4 days, mice were euthanized and the orthotopic melanomas were collected and digested by collagenase IV (Sangon Biotech), and leukocytes were isolated by 40 to 70% Percoll (GE) gradient centrifugation.

To measure the effector function of adoptively transferred cells (pmel-1 CD8$^+$ T-Tre/BCN-Lipo-Ava cells), isolated cells were stimulated with 1 μM ionomycin (MedChemExpress) and phorbol 12-myristate 13-acetate (50 ng/ml) for 4 hours in the presence of brefeldin A (5 μg/ml), followed by staining with phycoerythrin (PE)–Cy7 anti-mouse Thy1.1 (1 μg/ml; Thermo Fisher Scientific). Then, the cells were divided into three groups and stained with allophycocyanin (APC) anti-mouse PD-1 (0.4 μg/ml; Thermo Fisher Scientific), APC anti-mouse TIGIT (Vstm3) (0.4 μg/ml; BioLegend), or APC anti-mouse CD366 (TIM-3) (0.4 μg/ml; BioLegend). Next, cells were fixed with 4% PFA and permeabilized using 0.2% Triton X-100. After that, the cells were stained with FITC anti-mouse GzmB (1 μg/ml; BioLegend), PE-Cy5.5 anti-mouse IFNγ (0.6 μg/ml; BioLegend), or PE anti-mouse TNFα (0.5 μg/ml; BioLegend). To gate the cytokine- or granule-producing cells, T cells without stimulation or stained with isotype control antibody were used as negative controls for flow cytometry analysis. In a separate experiment, cells were stained with PE-Cy7 anti-mouse Thy1.1 (1 μg/ml). Then, the cells were divided into two groups and stained with APC anti-mouse PD-1 (0.4 μg/ml) (CD279) and PE anti-mouse TIGIT (Vstm3) (0.4 μg/ml; BioLegend), or APC anti-mouse CD366 (TIM-3) (0.4 μg/ml), PE anti-mouse CD152 (CTLA-4) (0.6 μg/ml; Thermo Fisher Scientific), and FITC anti-mouse CD223 (LAG-3) (0.6 μg/ml; Thermo Fisher Scientific) and analyzed by flow cytometry. To measure the proliferation and the amount of membrane cholesterol, isolated cells were stained with PE-Cy7 anti-mouse Thy1.1 (CD90.1) (1 μg/ml), PE anti-mouse Ki67 (0.6 μg/ml; BioLegend), and Filipin III (50 μg/ml; Santa Cruz Biotechnology), followed by analysis using flow cytometry.

To measure the effector function of tumor-infiltrating CD8$^+$ T cells, the isolated cells were first stimulated as above and then stained with APC-Cy7 anti-mouse CD8α (1 μg/ml; BD Pharmingen). Next, cells were fixed with 4% PFA and permeabilized with 0.2% Triton X-100. Then, the cells were stained with FITC anti-mouse GzmB (1 μg/ml; BioLegend), APC anti-mouse IFNγ (0.6 μg/ml; BioLegend), or PE anti-mouse TNFα (0.5 μg/ml; BioLegend). To gate the cytokine- or granule-producing cells, T cells without stimulation or stained with isotype control antibody were used as negative controls. To evaluate T cell exhaustion, isolated cells were stained with APC-Cy7 anti-mouse CD8α (CD90.1) (1 μg/ml), then divided into two groups, and stained with APC anti-mouse PD-1 (CD279) (0.4 μg/ml) and PE anti-mouse TIGIT (Vstm3) antibody (0.4 μg/ml), or APC anti-mouse CD366 (TIM-3) (0.4 μg/ml), PE anti-mouse CD152 (CTLA-4) (0.6 μg/ml), and FITC anti-mouse CD223 (LAG-3) (0.6 μg/ml), and then analyzed by flow cytometry. To measure the proliferation and the amount of membrane cholesterol, the isolated cells were stained with APC-Cy7 anti-mouse CD8α (1 μg/ml), PE anti-mouse Ki67 (0.6 μg/ml; BioLegend), and Filipin III (50 μg/ml; Santa Cruz Biotechnology), followed by analysis using flow cytometry.

Statistical analysis

Statistical analyses were performed using GraphPad Prism 8.0. All plots show means ± SEM. A one-way analysis of variance (ANOVA) test with Tukey's correction for multiple comparisons was used for comparisons of three or more groups. A Student's unpaired t test was used for two-group comparisons in the appropriate conditions. A log-rank (Mantel-Cox) test was used to analyze survival differences. Statistical significance was set at $^*P < 0.05$, $^{**}P < 0.01$, and $^{***}P < 0.001$, and ns denotes no significant difference.

SUPPLEMENTARY MATERIALS

stm.sciencemag.org/cgi/content/full/12/571/eaaz6667/DC1
Materials and Methods
Fig. S1. Synthesis of DSPE-BCN, DSPE-PEG$_{5k}$-Tre, DSPE-PEG$_{5k}$-Tre-FITC, and DSPE-PEG$_{5k}$-FITC.
Fig. S2. Characteristics of the click reaction and the liposomal Ava (BCN-Lipo-Ava).
Fig. S3. In vitro cytotoxicity and optimization of anchoring and clicking concentration and time.
Fig. S4. Percentage of anchoring liposomes on T cells over time.
Fig. S5. Surface anchor-engineered T cells maintained normal viability.
Fig. S6. Ava retention of surface anchor-engineered T-Tre/BCN-Lipo-Ava cells after transwell migration.
Fig. S7. In vitro activation of surface anchor-engineered T cells.
Fig. S8. The basal energy metabolism of surface anchor-engineered T cells.
Fig. S9. TMT-based quantitative proteomics of surface anchor-engineered T cells (T-Tre/BCN-Lipo cells).
Fig. S10. The abundance of ACAT1 proteins and the cytotoxicity of Ava in different types of cancer cells.
Fig. S11. Plasma membrane cholesterol concentration in T-Tre/BCN-Lipo-Ava cells over time.
Fig. S12. RNA expression of cholesterol metabolic genes in surface anchor-engineered T cells.
Fig. S13. IFNγ, TNFα, and GzmB production and cytotoxicity of CD8$^+$ T cells after adding or depleting cholesterol.
Fig. S14. Immunoblotting quantification of proximal and downstream TCR signaling molecules after stimulation with anti-CD3/CD28 antibodies.
Fig. S15. The population of pmel-1 CD8$^+$ T cells and accumulation of Ava in tumors after injection of pmel-1 T-Tre/BCN-Lipo-Ava cells.
Fig. S16. Safety evaluation of heart tissue by microscopic pathological analysis in B16F10 orthotopic melanoma mouse model.
Fig. S17. Safety evaluation of liver tissue by microscopic pathological analysis in B16F10 orthotopic melanoma mouse model.
Fig. S18. Safety evaluation of spleen tissue by microscopic pathological analysis in B16F10 orthotopic melanoma mouse model.
Fig. S19. Safety evaluation of lung tissue by microscopic pathological analysis in B16F10 orthotopic melanoma mouse model.
Fig. S20. Safety evaluation of kidney tissue by microscopic pathological analysis in B16F10 orthotopic melanoma mouse model.
Fig. S21. Biosafety analysis of surface anchor-engineered pmel-1 T cells in B16F10 orthotopic melanoma.
Fig. S22. Antitumor efficacy of OT-I T-Tre/BCN-Lipo-Ava cells in B16F10-OVA orthotopic melanoma mouse model.
Fig. S23. Biosafety analysis of surface anchor-engineered OT-I T cells in B16F10-OVA orthotopic melanoma.
Fig. S24. Characterization of tumor-infiltrating CD8$^+$ T cells after pmel-1 T-Tre/BCN-Lipo-Ava cell transfer in B16F10 orthotopic tumors.
Fig. S25. IFNγ, TNFα, and GzmB production of tumor-infiltrating CD8$^+$ T cells after OT-I T-Tre/BCN-Lipo-Ava cell transfer in B16F10-OVA orthotopic tumors.
Fig. S26. The exhaustion and immunosuppressive status of pmel-1 T-Tre/BCN-Lipo-Ava cells and tumor-infiltrating CD8$^+$ T cells after a single transfer in B16F10 orthotopic tumors.
Fig. S27. Pathology analysis of pulmonary sections of B16F10-OVA lung disseminated melanoma model.
Fig. S28. Biosafety analysis of surface anchor-engineered OT-I T cells in a B16F10-OVA lung disseminated melanoma model.
Fig. S29. IFNγ, TNFα, and GzmB production of tumor-infiltrating CD8$^+$ T cells after OT-I T-Tre/BCN-Lipo-Ava cell transfer in a B16F10-OVA lung disseminated melanoma model.
Fig. S30. Characteristics of LN-229 glioblastoma cells.
Fig. S31. Characteristics of anti–GD-2 CAR T cells.
Fig. S32. Surface-anchoring of GD-2 CAR T cells by liposomal Ava enhanced TCR clustering and immunological synapse formation.
Table S1. The number of liposomes anchored on the surface of T cells.
Data file S1. Raw data for Figs. 1 to 7.
Data file S2. Raw data for figs. S2 to S29.

View/request a protocol for this paper from *Bio-protocol*.

REFERENCES AND NOTES

1. A. L. Garfall, M. V. Maus, W. T. Hwang, S. F. Lacey, Y. D. Mahnke, J. J. Melenhorst, Z. Zheng, D. T. Vogl, A. D. Cohen, B. M. Weiss, K. Dengel, N. D. Kerr, A. Bagg, B. L. Levine, C. H. June, E. A. Stadtmauer, Chimeric antigen receptor T cells against CD19 for multiple myeloma. *N. Engl. J. Med.* **373**, 1040–1047 (2015).

2. S. A. Grupp, M. Kalos, D. Barrett, R. Aplenc, D. L. Porter, S. R. Rheingold, D. T. Teachey, A. Chew, B. Hauck, J. F. Wright, M. C. Milone, B. L. Levine, C. H. June, Chimeric antigen receptor–modified T cells for acute lymphoid leukemia. *N. Engl. J. Med.* **368**, 1509–1518 (2013).
3. E. K. Moon, L.-C. Wang, D. V. Dolfi, C. B. Wilson, R. Ranganathan, J. Sun, V. Kapoor, J. Scholler, E. Puré, M. C. Milone, C. H. June, J. L. Riley, E. J. Wherry, S. M. Albelda, Multifactorial T-cell hypofunction that is reversible can limit the efficacy of chimeric antigen receptor–transduced human T cells in solid tumors. *Clin. Cancer Res.* **20**, 4262–4273 (2014).
4. A. Ribas, J. D. Wolchok, Cancer immunotherapy using checkpoint blockade. *Science* **359**, 1350–1355 (2018).
5. J. Tang, L. Pearce, J. O'Donnell-Tormey, V. M. Hubbard-Lucey, Trends in the global immuno-oncology landscape. *Nat. Rev. Drug Discov.* **17**, 783–784 (2018).
6. J. Tang, A. Shalabi, V. M. Hubbard-Lucey, Comprehensive analysis of the clinical immuno-oncology landscape. *Ann. Oncol.* **29**, 84–91 (2018).
7. J. Li, W. Li, K. Huang, Y. Zhang, G. Kupfer, Q. Zhao, Chimeric antigen receptor T cell (CAR-T) immunotherapy for solid tumors: Lessons learned and strategies for moving forward. *J. Hematol. Oncol.* **11**, 22 (2018).
8. T. Gargett, W. Yu, G. Dotti, E. S. Yvon, S. N. Christo, J. D. Hayball, I. D. Lewis, M. K. Brenner, M. P. Brown, GD2-specific CAR T cells undergo potent activation and deletion following antigen encounter but can be protected from activation-induced cell death by PD-1 blockade. *Mol. Ther.* **24**, 1135–1149 (2016).
9. G. Varricchi, M. R. Galdiero, V. Mercurio, D. Bonaduce, G. Marone, C. G. Tocchetti, Pharmacovigilating cardiotoxicity of immune checkpoint inhibitors. *Lancet Oncol.* **19**, 1545–1546 (2018).
10. P. F. Wang, Y. Chen, S.-Y. Song, T.-J. Wang, W.-J. Ji, S.-W. Li, N. Liu, C.-X. Yan, Immune-related adverse events associated with Anti-PD-1/PD-L1 treatment for malignancies: A meta-analysis. *Front. Pharmacol.* **8**, 730 (2017).
11. K. Renner, K. Singer, G. E. Koehl, E. K. Geissler, K. Peter, P. J. Siska, M. Kreutz, Metabolic hallmarks of tumor and immune cells in the tumor microenvironment. *Front. Immunol.* **8**, 248 (2017).
12. C.-H. Chang, E. L. Pearce, Emerging concepts of T cell metabolism as a target of immunotherapy. *Nat. Immunol.* **17**, 364–368 (2016).
13. E. Molnár, M. Swamy, M. Holzer, K. Beck-García, R. Worch, C. Thiele, G. Guigas, K. Boye, I. F. Luescher, P. Schwille, R. Schubert, W. W. A. Schamel, Cholesterol and sphingomyelin drive ligand-independent T-cell antigen receptor nanoclustering. *J. Biol. Chem.* **287**, 42664–42674 (2012).
14. W. W. A. Schamel, I. Arechaga, R. M. Risueño, H. M. van Santen, P. Cabezas, C. Risco, J. M. Valpuesta, B. Alarcón, Coexistence of multivalent and monovalent TCRs explains high sensitivity and wide range of response. *J. Exp. Med.* **202**, 493–503 (2005).
15. T. Zech, C. S. Ejsing, K. Gaus, B. de Wet, A. Shevchenko, K. Simons, T. Harder, Accumulation of raft lipids in T-cell plasma membrane domains engaged in TCR signalling. *EMBO J.* **28**, 466–476 (2009).
16. W. Yang, Y. Bai, Y. Xiong, J. Zhang, S. Chen, X. Zheng, X. Meng, L. Li, J. Wang, C. Xu, C. Yan, L. Wang, C. C. Y. Chang, T.-Y. Chang, T. Zhang, P. Zhou, B.-L. Song, W. Liu, S.-c. Sun, X. Liu, B.-l. Li, C. Xu, Potentiating the antitumour response of $CD8^+$ T cells by modulating cholesterol metabolism. *Nature* **531**, 651–655 (2016).
17. I. A. Khawar, J. H. Kim, H.-J. Kuh, Improving drug delivery to solid tumors: Priming the tumor microenvironment. *J. Control. Release* **201**, 78–89 (2015).
18. M. C. Milone, V. G. Bhoj, The pharmacology of T cell therapies. *Mol. Ther. Meth. Clin. Dev.* **8**, 210–221 (2018).
19. M. Norelli, M. Casucci, C. Bonini, A. Bondanza, Clinical pharmacology of CAR-T cells: Linking cellular pharmacodynamics to pharmacokinetics and antitumor effects. *Biochim. Biophys. Acta* **1865**, 90–100 (2016).
20. G. Llaverías, J. C. Laguna, M. Alegret, Pharmacology of the ACAT inhibitor avasimibe (CI-1011). *Cardiovasc. Drug Rev.* **21**, 33–50 (2003).
21. B. Heemskerk, K. Liu, M. E. Dudley, L. A. Johnson, A. Kaiser, S. Downey, Z. Zheng, T. E. Shelton, K. Matsuda, P. F. Robbins, R. A. Morgan, S. A. Rosenberg, Adoptive cell therapy for patients with melanoma, using tumor-infiltrating lymphocytes genetically engineered to secrete interleukin-2. *Hum. Gene Ther.* **19**, 496–510 (2008).
22. K. Adachi, Y. Kano, T. Nagai, N. Okuyama, Y. Sakoda, K. Tamada, IL-7 and CCL19 expression in CAR-T cells improves immune cell infiltration and CAR-T cell survival in the tumor. *Nat. Biotechnol.* **36**, 346–351 (2018).
23. S. Rafiq, O. O. Yeku, H. J. Jackson, T. J. Purdon, D. G. van Leeuwen, D. J. Drakes, M. Song, M. M. Miele, Z. Li, P. Wang, S. Yan, J. Xiang, X. Ma, V. E. Seshan, R. C. Hendrickson, C. Liu, R. J. Brentjens, Targeted delivery of a PD-1-blocking scFv by CAR-T cells enhances anti-tumor efficacy *in vivo*. *Nat. Biotechnol.* **36**, 847–856 (2018).
24. C. Zhang, J. Liu, J. F. Zhong, X. Zhang, Engineering CAR-T cells. *Biomark. Res.* **5**, 22 (2017).
25. M. C. Milone, U. O'Doherty, Clinical use of lentiviral vectors. *Leukemia* **32**, 1529–1541 (2018).
26. H. Pan, P. Li, G. Li, W. Li, B. Hu, H. He, Z. Chen, F. Wang, L. Liu, Y. Gong, Y. Han, Y. Luo, M. Zheng, Y. Ma, L. Cai, Y. Jin, Glycometabolic bioorthogonal chemistry-guided viral transduction for robust human T cell engineering. *Adv. Funct. Mater.* **29**, 1807528 (2019).
27. M. T. Stephan, J. J. Moon, S. H. Um, A. Bershteyn, D. J. Irvine, Therapeutic cell engineering with surface-conjugated synthetic nanoparticles. *Nat. Med.* **16**, 1035–1041 (2010).
28. L. Tang, Y. Zheng, M. B. Melo, L. Mabardi, A. P. Castaño, Y.-Q. Xie, N. Li, S. B. Kudchodkar, H. C. Wong, E. K. Jeng, M. V. Maus, D. J. Irvine, Enhancing T cell therapy through TCR-signaling-responsive nanoparticle drug delivery. *Nat. Biotechnol.* **36**, 707–716 (2018).
29. M. T. Stephan, S. B. Stephan, P. Bak, J. Z. Chen, D. J. Irvine, Synapse-directed delivery of immunomodulators using T-cell-conjugated nanoparticles. *Biomaterials* **33**, 5776–5787 (2012).
30. B. N. Huang, W. D. Abraham, Y. R. Zheng, S. C. B. López, S. S. Luo, D. J. Irvine, Active targeting of chemotherapy to disseminated tumors using nanoparticle-carrying T cells. *Sci. Transl. Med.* **7**, 291ra94 (2015).
31. W. J. Li, H. Pan, H. He, X. Meng, Q. Ren, P. Gong, X. Jiang, Z. Liang, L. Liu, M. Zheng, X. Shao, Y. Ma, L. Cai, Bio-orthogonal T cell targeting strategy for robustly enhancing cytotoxicity against tumor cells. *Small* **15**, e1804383 (2019).
32. M. G. Paulick, C. R. Bertozzi, The glycosylphosphatidylinositol anchor: A complex membrane–anchoring structure for proteins. *Biochemistry* **47**, 6991–7000 (2008).
33. S. Nagarajan, P. Selvaraj, Glycolipid-anchored IL-12 expressed on tumor cell surface induces antitumor immune response. *Cancer Res.* **62**, 2869–2874 (2002).
34. I. Nikić, J. H. Kang, G. E. Girona, I. V. Aramburu, E. A. Lemke, Labeling proteins on live mammalian cells using click chemistry. *Nat. Protoc.* **10**, 780–791 (2015).
35. J. Xue, Z. Zhao, L. Zhang, L. Xue, S. Shen, Y. Wen, Z. Wei, L. Wang, L. Kong, H. Sun, Q. Ping, R. Mo, C. Zhang, Neutrophil-mediated anticancer drug delivery for suppression of postoperative malignant glioma recurrence. *Nat. Nanotechnol.* **12**, 692–700 (2017).
36. L. Dupré, R. Houmadi, C. Tang, J. Rey-Barroso, T lymphocyte migration: An action movie starring the actin and associated actors. *Front. Immunol.* **6**, 586 (2015).
37. M. Santamaria, M. Marubayashi, J.-M. Arizon, A. Montero, M. Concha, F. Valles, A. Lopez, F. Lopez, J. Peña, The activation antigen CD69 is selectively expressed on CD8+ endomyocardium infiltrating T lymphocytes in human rejecting heart allografts. *Hum. Immunol.* **33**, 1–4 (1992).
38. S. F. Ziegler, F. Ramsdell, M. R. Alderson, The activation antigen CD69. *Stem Cells* **12**, 456–465 (1994).
39. M. del Carmen Castellanos, S. López-Giral, M. López-Cabrera, M. O. de Landázuri, Multiple cis-acting elements regulate the expression of the early T cell activation antigen CD69. *Eur. J. Immunol.* **32**, 3108–3117 (2002).
40. W. W. Overwijk, A. Tsung, K. R. Irvine, M. R. Parkhurst, T. J. Goletz, K. Tsung, M. W. Carroll, C. Liu, B. Moss, S. A. Rosenberg, N. P. Restifo, gp100/pmel 17 is a murine tumor rejection antigen: Induction of "Self"-reactive, tumoricidal T cells using high-affinity, altered peptide ligand. *J. Exp. Med.* **188**, 277–286 (1998).
41. J. Fan, R. Lin, S. Xia, D. Chen, S. E. Elf, S. Liu, Y. Pan, H. Xu, Z. Qian, M. Wang, C. Shan, L. Zhou, Q.-Y. Lei, Y. Li, H. Mao, B. H. Lee, J. Sudderth, R. J. De Berardinis, G. Zhang, T. Owonikoko, M. Gaddh, M. L. Arellano, H. J. Khoury, F. R. Khuri, S. Kang, P. W. Doetsch, S. Lonial, T. J. Boggon, W. J. Curran, J. Chen, Tetrameric acetyl-CoA acetyltransferase 1 is important for tumor growth. *Mol. Cell* **64**, 859–874 (2016).
42. N. E. Scharping, A. V. Menk, R. S. Moreci, R. D. Whetstone, R. E. Dadey, S. C. Watkins, R. L. Ferris, G. M. Delgoffe, The tumor microenvironment represses T cell mitochondrial biogenesis to drive intratumoral T cell metabolic insufficiency and dysfunction. *Immunity* **45**, 374–388 (2016).
43. A. Heczey, D. Liu, G. Tian, A. N. Courtney, J. Wei, E. Marinova, X. Gao, L. Guo, E. Yvon, J. Hicks, H. Liu, G. Dotti, L. S. Metelitsa, Invariant NKT cells with chimeric antigen receptor provide a novel platform for safe and effective cancer immunotherapy. *Blood* **124**, 2824–2833 (2014).
44. L. Zhang, P. Romero, Metabolic control of $CD8^+$ T cell fate decisions and antitumor Immunity. *Trends Mol. Med.* **24**, 30–48 (2018).
45. J. G. Crompton, M. Sukumar, R. Roychoudhuri, D. Clever, A. Gros, R. L. Eil, E. Tran, K.-I. Hanada, Z. Yu, D. C. Palmer, S. P. Kerkar, R. D. Michalek, T. Upham, A. Leonardi, N. Acquavella, E. Wang, F. M. Marincola, L. Gattinoni, P. Muranski, M. S. Sundrud, C. A. Klebanoff, S. A. Rosenberg, D. T. Fearon, N. P. Restifo, Akt inhibition enhances expansion of potent tumor-specific lymphocytes with memory cell characteristics. *Cancer Res.* **75**, 296–305 (2015).
46. L. Gattinoni, C. A. Klebanoff, D. C. Palmer, C. Wrzesinski, K. Kerstann, Z. Yu, S. E. Finkelstein, M. R. Theoret, S. A. Rosenberg, N. P. Restifo, Acquisition of full effector function in vitro paradoxically impairs the in vivo antitumor efficacy of adoptively transferred CD8+ T cells. *J. Clin. Invest.* **115**, 1616–1626 (2005).
47. D. O'Sullivan, E. L. Pearce, Targeting T cell metabolism for therapy. *Trends Immunol.* **36**, 71–80 (2015).
48. C. M. Alvey, K. R. Spinler, J. Irianto, C. R. Pfeifer, B. Hayes, Y. Xia, S. Cho, P. C. P. D. Dingal, J. Hsu, L. Smith, M. Tewari, D. E. Discher, SIRPA-inhibited, marrow-derived macrophages engorge, accumulate, and differentiate in antibody-targeted regression of solid tumors. *Curr. Biol.* **27**, 2065–2077.e6 (2017).
49. J. A. Hubbell, A. Chilkoti, Nanomaterials for drug delivery. *Science* **337**, 303–305 (2012).
50. R. A. Petros, J. M. DeSimone, Strategies in the design of nanoparticles for therapeutic applications. *Nat. Rev. Drug Discov.* **9**, 615–627 (2010).

51. E. Blanco, H. Shen, M. Ferrari, Principles of nanoparticle design for overcoming biological barriers to drug delivery. *Nat. Biotechnol.* **33**, 941–951 (2015).
52. S. T. Hess, T. J. Gould, M. V. Gudheti, S. A. Maas, K. D. Mills, J. Zimmerberg, Dynamic clustered distribution of hemagglutinin resolved at 40 nm in living cell membranes discriminates between raft theories. *Proc. Natl. Acad. Sci. U.S.A.* **104**, 17370–17375 (2007).
53. S. T. Hess, M. Kumar, A. Verma, J. Farrington, A. Kenworthy, J. Zimmerberg, Quantitative electron microscopy and fluorescence spectroscopy of the membrane distribution of influenza hemagglutinin. *J. Cell Biol.* **169**, 965–976 (2005).
54. Y. Han, H. Pan, W. Li, Z. Chen, A. Ma, T. Yin, R. Liang, F. Chen, Y. Ma, Y. Jin, M. Zheng, B. Li, L. Cai, T cell membrane mimicking nanoparticles with bioorthogonal targeting and immune recognition for enhanced photothermal therapy. *Adv. Sci.* **6**, 1900251 (2019).
55. C.-M. J. Hu, R. H. Fang, K.-C. Wang, B. T. Luk, S. Thamphiwatana, D. Dehaini, P. Nguyen, P. Angsantikul, C. H. Wen, A. V. Kroll, C. Carpenter, M. Ramesh, V. Qu, S. H. Patel, J. Zhu, W. Shi, F. M. Hofman, T. C. Chen, W. Gao, K. Zhang, S. Chien, L. Zhang, Nanoparticle biointerfacing by platelet membrane cloaking. *Nature* **526**, 118–121 (2015).
56. C. E. Brown, B. Aguilar, R. Starr, X. Yang, W.-C. Chang, L. Weng, B. Chang, A. Sarkissian, A. Brito, J. F. Sanchez, J. R. Ostberg, M. D'Apuzzo, B. Badie, M. E. Barish, S. J. Forman, Optimization of IL13Rα2-targeted chimeric antigen receptor T cells for improved anti-tumor efficacy against glioblastoma. *Mol. Ther.* **26**, 31–44 (2018).

Acknowledgments: We thank the Public Platform of the State Key Laboratory of Natural Medicines for assistance with the pathological-section imaging and flow cytometry, and we are grateful to Y. Shen and P. Zhou for help in performing FACS experiments. In addition, we thank M. Ding for assistance with the proteomics testing and analysis. **Funding:** This work was supported by the National Natural Science Foundation of China (81930099 to C.Z., 81773664 to C.Z., 81473153 to C.Z., and 81903651 to S.H.), "Double First-Class" University project (CPU2018GY47 to C.Z. and CPU2018GF10 to C.Z.), China Postdoctoral Science Foundation funded project (2017 M611956 to S.H.), Natural Science Foundation of Jiangsu Province (BK20190558 to M.H. and BK20180565 to S.H.), 111 Project from the Ministry of Education of China and the State Administration of Foreign Expert Affairs of China (no. 111-2-07 to C.Z. and B17047 to C.Z.), and the Open Project of State Key Laboratory of Natural Medicines (no. SKLNMZZ202017 to C.Z.). **Author contributions:** M.H. designed and conducted all experiments, analyzed the data, and wrote the manuscript. S.H. designed and conducted all cell and animal experiments, analyzed the data, and wrote the manuscript. W.L. analyzed the data and wrote the manuscript. K.L. assisted in in vivo pharmacodynamic experiments and Western blot analysis. L.X. assisted in data analysis. Q.H. and L.Z. assisted in the genetic identification and breeding of C57BL/6J pmel-1 mice and C57BL/6J OT-I mice. Y.C. assisted in the synthesis of DSPE-BCN. H.S. supervised the metabolic experiments. C.J. supervised all animal experiments and wrote the manuscript. C.Z. conceived the project and supervised all experiments. **Competing interests:** The authors declare that they have no competing interests. **Data and materials availability:** All data associated with this study are present in the paper or the Supplementary Materials.

Submitted 28 September 2019
Resubmitted 14 July 2020
Accepted 21 August 2020
Published 25 November 2020
10.1126/scitranslmed.aaz6667

Citation: M. Hao, S. Hou, W. Li, K. Li, L. Xue, Q. Hu, L. Zhu, Y. Chen, H. Sun, C. Ju, C. Zhang, Combination of metabolic intervention and T cell therapy enhances solid tumor immunotherapy. *Sci. Transl. Med.* **12**, eaaz6667 (2020).

Science Translational Medicine

Combination of metabolic intervention and T cell therapy enhances solid tumor immunotherapy

Meixi Hao, Siyuan Hou, Weishuo Li, Kaiming Li, Lingjing Xue, Qifan Hu, Lulu Zhu, Yue Chen, Hongbin Sun, Caoyun Ju and Can Zhang

Sci Transl Med **12**, eaaz6667.
DOI: 10.1126/scitranslmed.aaz6667

Reprogramming T cell metabolism with a click

Cancer therapies in which tumor-specific T cells are transferred into a patient often fail to control solid tumors. This is partially due to metabolic dysfunction of the transferred T cells at the tumor site. In this study, Hao *et al*. reprogrammed T cells by anchoring, and clicking, a drug that modulates metabolism to the surface of the T cells. This drug, avasimibe, increased cholesterol in the T cell membrane, which enhanced T cell activation, promoted tumor cell killing, and extended survival in mouse models of melanoma and glioblastoma. Thus, using click chemistry to anchor drugs on the surface of T cells may be a useful technique to improve functionality of adoptive T cell therapies.

ARTICLE TOOLS	http://stm.sciencemag.org/content/12/571/eaaz6667
SUPPLEMENTARY MATERIALS	http://stm.sciencemag.org/content/suppl/2020/11/23/12.571.eaaz6667.DC1
RELATED CONTENT	http://stm.sciencemag.org/content/scitransmed/12/565/eabb0152.full http://stm.sciencemag.org/content/scitransmed/12/559/eaaz1863.full http://stm.sciencemag.org/content/scitransmed/11/499/eaau5907.full http://stm.sciencemag.org/content/scitransmed/11/495/eaaw2293.full http://stm.sciencemag.org/content/scitransmed/12/533/eaaw2672.full
REFERENCES	This article cites 56 articles, 13 of which you can access for free http://stm.sciencemag.org/content/12/571/eaaz6667#BIBL
PERMISSIONS	http://www.sciencemag.org/help/reprints-and-permissions

Science Translational Medicine (ISSN 1946-6242) is published by the American Association for the Advancement of Science, 1200 New York Avenue NW, Washington, DC 20005. The title *Science Translational Medicine* is a registered trademark of AAAS.